

# Comparison of Microstructure Refinement in Wire-Arc Additively Manufactured Ti-6Al-2Sn-4Zr-2Mo-0.1Si and Ti-6Al-4V Built With Inter-Pass Deformation



A.E. DAVIS, A.E. CABALLERO, R. BISWAL, S. WILLIAMS, and P.B. PRANGNELL

The titanium alloy Ti-6Al-2Sn-4Zr-2Mo-0.1Si (Ti6242) has been deposited for the first time by a directed energy deposition process using a wire and arc system—*i.e.*, wire-arc additive manufacturing (WAAM)—with and without inter-pass machine hammer peening, and its microstructure investigated and compared to the more commonly used alloy Ti-6Al-4V (Ti64). The application of inter-pass machine hammer peening—where each added layer was deformed before deposition—successfully refined the strongly textured, coarse, columnar  $\beta$ -grain structure that is commonly seen in  $\alpha + \beta$  titanium alloys, producing a finer equiaxed grain structure with a near-random  $\alpha$  texture. The average grain diameter and texture strength decreased with the peening pitch. When Ti6242 was deposited under identical conditions to Ti64, by switching the alloy feed wire in-situ, the refined  $\beta$ -grain size decreased across the alloy-to-alloy transition reaching on average 25 pct less in Ti6242 than in Ti64. A similar 25 pct scale reduction was also found in the Ti6242  $\alpha$ -lath transformation microstructure. This comparatively greater microstructure refinement in Ti6242 was attributed to the dissimilar alloying elements present in the two materials; specifically, molybdenum, which has a lower diffusivity than vanadium and led to slower  $\beta$ -grain growth during reheating as well as a finer transformation microstructure.

<https://doi.org/10.1007/s11661-022-06811-1>

© The Author(s) 2022

## I. INTRODUCTION

ADDITIVE manufacturing (AM) of high-value titanium near-net-shape parts offers the potential for significant cost and energy savings over conventional wrought components with low production volumes<sup>[1–3]</sup> and has consequently attracted attention from the aerospace industry. Of particular interest to manufacturing larger airframe components are wire-fed high-deposition-rate directed-energy-deposition (DED) processes, like wire-arc AM (WAAM), that are capable of kilogram-per-hour deposition rates and build envelopes of several metres. Parts manufactured by AM are also more geometrically adaptable and have shorter lead times compared to forgings.<sup>[1,2]</sup> However, with high-deposition-rate processes, as-deposited microstructure

heterogeneity is generally more pronounced than in finer-scale powder-bed systems,<sup>[2,4,5]</sup> because it is exacerbated by the larger heat source and layer height, and resultant lower solidification and cooling rates.<sup>[6–13]</sup> The coarser grain structures and more pronounced heat affected zone (HAZ) banding features found in WAAM, with the most common ‘workhorse’ titanium alloy, Ti-6Al-4V (Ti64) are well documented and much of the recent research in this area has focused on combating this microstructure heterogeneity and resultant mechanical anisotropy.<sup>[5,12–21]</sup>

The coarse, columnar, and strongly textured  $\beta$ -grain structures that form in WAAM during deposition under normal processing conditions<sup>[13,17,22,23]</sup> can result in anisotropic mechanical properties<sup>[13,17,19]</sup> and less predictable damage tolerance.<sup>[24,25]</sup> In alloys like Ti64, these less desirable  $\beta$ -grain structures that develop during deposition arise due to a lack of nucleation in the melt pool ahead of the solidification front. The columnar grains grow epitaxially through multiple deposited layers, reaching millimetres in size, and exhibit a strong  $\langle 001 \rangle_{\beta}$  fibre texture.<sup>[20,22,23]</sup> This lack of nucleation at the solidification front stems primarily from the low partitioning of the main alloying elements, Al and V, in Ti64<sup>[26,27]</sup> and a resultant lack of constitutional undercooling.<sup>[28]</sup> Recently, various methods of refining the

A.E. DAVIS and P.B. PRANGNELL are with the Department of Materials, The University of Manchester, Manchester M13 9PL, UK. Contact e-mail: alec.davis@manchester.ac.uk A.E. CABALLERO, R. BISWAL and S. WILLIAMS are with the Welding Engineering and Laser Processing Centre, Cranfield University, Bedfordshire MK43 0PL, UK.

Manuscript submitted May 16, 2022; accepted July 31, 2022.

Article published online September 22, 2022

columnar  $\beta$ -grain structure and weakening the texture have been developed, which include applying novel techniques such as:

- *Inter-pass deformation*: where each individual as-deposited layer is cold worked by rolling or peening, between deposition passes, resulting in recrystallisation of the  $\beta$  grains when reheating during deposition of the next layer.<sup>[17,19,23,29,30]</sup>
- *Ultrasonic melt pool agitation*: where high-energy ultrasound is used to stimulate grain nucleation in the melt pool by acoustic cavitation.<sup>[18]</sup>
- *Alloy modification*: where trace elements are added to either promote solutal growth restriction,<sup>[31,32]</sup> or increase nucleation at low undercoolings through inoculation.<sup>[21,33,34]</sup>

Unfortunately, these methods all have intrinsic associated complications such as the challenges and additional cost of implementing the techniques (*e.g.*, inter-pass deformation and ultrasonic agitation) or the introduction of unwanted, brittle, intermetallic particles and the requirement for alloy requalification, as a result of alloy modification.

In addition, other studies have shown that it may be possible to promote grain nucleation by crossing the *columnar to equiaxed transition (CET)* line, through more intelligent control of the deposition parameters, to produce a higher solidification rate combined with a low liquid thermal gradient at the solidification front.<sup>[14,35]</sup> However, this approach may not be as compatible with achieving a stable process from the viewpoint of geometrical accuracy.

$\alpha + \beta$  and near- $\alpha$  titanium alloys, like Ti64 and Ti-6Al-2Sn-4Zr-2Mo-0.1Si (Ti6242) have a high  $\alpha$ -phase stability and exhibit relatively rapid diffusional  $\beta \rightarrow \alpha$  transformation kinetics.<sup>[36]</sup> As a result, during thermal cycling in the WAAM process, where each deposited layer is reheated multiple times with a decreasing peak temperature, several full and partial transformations between  $\alpha$  and  $\beta$  phases can occur. Initially, when the material is reheated above the  $\beta$  transus ( $T_\beta$ ) it transforms on cooling to fine basketweave lamellar  $\alpha$ , due to the relatively high cooling rates ( $\sim 10^2$  °C s<sup>-1</sup><sup>[5,15]</sup>). However, where this material is then reheated locally into the range of the  $\beta$ -phase approach curve, heat affected zone (HAZ) bands form.<sup>[5,15,16]</sup> In Ti64, the HAZ bands develop following a locus of the  $\sim 800$  °C to 1000 °C peak temperature range reached in the thermal gradient that is generated below the translated heat source,<sup>[5,15,16,30]</sup> and present as regularly spaced, horizontal lines in single-wire-bead WAAM walls and with a curved 'fish-scale' pattern in multi-pass bead deposits.<sup>[12-16,25]</sup> They are visible in etched optical micrographs due to the contrast caused by the coarsening of the  $\alpha$  microstructure, which is combined with increased solute partitioning towards the top of each band.<sup>[5,14,16]</sup> A further consequence of HAZ banding is the formation of a repeating 'sawtooth' wave profile in the  $\alpha$  inter-lamellar spacing across the deposited layers. This can be accompanied by a more gradual long-range increase in the

average inter-lamellar spacing if accumulation occurs in the background temperature.<sup>[5,15,16]</sup> When combined with the formation of grain-boundary  $\alpha$  colonies, and the locally heterogeneous micro-texture inherited by the Burgers orientation relationship (BOR) from the coarse parent  $\beta$  grains, this typically results in heterogeneous and anisotropic  $\alpha + \beta$  transformation microstructures in titanium as-deposited WAAM builds, which are known to affect their micromechanical behaviour<sup>[37]</sup>, for example, by impacting fatigue crack growth rates.<sup>[25,38]</sup>

Most titanium DED-AM research to date has focused on Ti64, but more recently, other alloys have been deposited and characterised (*e.g.*, Ti-5Al-5V-Mo-3Cr (Ti5553)<sup>[39]</sup> and Ti6242,<sup>[40,41]</sup>) to address more specialised aerospace applications, where alternative materials are preferred for their greater strength or high-temperature capability.<sup>[36]</sup> For example, Ti6242 is a high-temperature alloy that can be used up to  $\sim 540$  °C, whereas Ti64 is only recommended for applications below 350 °C.<sup>[36,42-44]</sup> Due to its different alloying elements, Ti6242 has a higher  $\alpha$ -phase stability compared to Ti64 (*i.e.*, the two alloy's 'molybdenum equivalence' index<sup>[45]</sup> are  $-5.3$  and  $-3.3$ , respectively) and retains less  $\beta$  phase, which, in conjunction with the additional solid-solution strengthening from Sn, Zr, and Si, maintains a higher yield strength at elevated temperatures and helps provide greater creep resistance.<sup>[36,42,43]</sup> In Ti6242, silicon promotes the formation of silicides during ageing heat treatments that nucleate on  $\alpha$ -lath boundaries to improve creep resistance; and the slower diffusing alloying element molybdenum provides further creep and oxidation resistance.<sup>[44,46,47]</sup> Burkhardt *et al.* and Harish<sup>[40,41]</sup> have deposited Ti6242 test samples with powder and wire laser-metal deposition, respectively, which show similar coarse and columnar  $\beta$ -grain structures and HAZ bands to those formed during deposition of Ti64 (*e.g.*, References 22, 23). However, to date, to the current authors' knowledge, little in-depth characterisation has been carried out on Ti6242 components produced by Wire-DED-AM, nor has the impact of thermal cycling during AM on the transformation microstructure been studied.

In this work, we have deposited several Ti6242 test samples using the high-deposition-rate WAAM process with inter-pass machine hammer peening, to investigate the level of refinement of the columnar  $\beta$ -grain structure that could be achieved by combining in-situ deformation by peening with WAAM. We have also studied the impact of thermal cycling on the  $\alpha + \beta$  transformation microstructure. These results were directly compared to a baseline Ti64 alloy, produced under exactly the same thermal conditions, by building alloy-alloy composite (AAC) samples consisting of Ti6242 deposited on top of Ti64. The sample microstructures were subsequently investigated with optical microscopy, and over large areas at high resolution by scanning electron microscopy (SEM) image mapping, combined with energy dispersive X-ray spectroscopy (EDS), and electron backscatter diffraction (EBSD), to obtain quantitative data of the scale and homogeneity of the alloys' respective grain and transformation microstructures. This allowed a

comparison to be made of their microstructure response to the dissimilar alloying elements present in the two materials.

## II. EXPERIMENTAL METHODS

### A. Materials and Build Parameters

Four 200 mm long and 50 mm high, single-track wide (10 mm) Ti6242 WAAM linear wall test samples were produced using the build parameters shown in Table I, with the travel direction rotated 180° between each deposition pass. During deposition, the temperature of the top layer was monitored and controlled so that it fell to 100 °C between each pass. The composition of the deposited Ti6242 material analysed by the inductively coupled plasma (ICP) technique, along with compositions of the wire consumables provided by the wire manufactures, are presented in Table II. All test walls were deposited on 12.7 mm-thick hot-rolled Ti64 substrates. One baseline wall was deposited without inter-pass deformation. The three other samples were peened across their top surface along the wall centre line after every layer was deposited, by traversing a pneumatic RRH06P Atlas Copco peening tool with a 10 mm radius spherical head using a robot, with an impact energy of 6 J, frequency of 25 Hz, and translation pitches of 0.4, 1.2, and 3.9 mm (giving translation speeds of the peening tool of 10, 30, and 100 mm s<sup>-1</sup>, respectively). The goal of varying the peening pitch, or the spacing between peening tool impact locations was to investigate the effect of changing the strain-field overlap and the average energy density applied to each layer.<sup>[30]</sup>

In addition, another 200 mm long and 72 mm high, single-track-wide (10 mm) wall was built to allow direct comparison of the microstructure of Ti6242 with that of Ti64 when deposited under *exactly* the same process conditions (Table I). This was achieved by first depositing a Ti64 wall to a height of 42 mm until steady state conditions were reached, and then switching the wire feed to Ti6242 and depositing another 30 mm to a total height of 72 mm. This AAC Ti64 → Ti6242 sample was peened every layer with a pitch of 0.4 mm except for a 50 mm long section at one end, which was left so that peened and un-peened regions could be directly compared in the same build. The inter-pass temperature was also increased slightly to 200 °C to raise the production rate for this larger sample. A schematic of this AAC WAAM build is shown in Figure 1(c).

### B. Macro and Microstructure Characterisation

The sample reference frame used throughout is defined in Figure 1(c) as: the heat source translation direction ≡ WD, the normal, or build height direction ≡ ND, and the transverse direction to the wall ≡ TD. Samples for metallographic examination were sectioned in the normal-transverse (ND-TD) plane and prepared

**Table I. WAAM Deposition Parameters**

WAAM Build Parameters	
Wire Feed Speed	2 m min <sup>-1</sup> (33 mm s <sup>-1</sup> )
Travel Speed	5 mm s <sup>-1</sup>
Wire Diameter	1.2 mm
Current	180 A
Plasma Gas Flow Rate	0.8 L min <sup>-1</sup>
Argon Shielding Gas Flow Rate	70 L min <sup>-1</sup>

using silicon carbide paper of reducing grit size down to 4000 grade, followed by a final polishing stage using a colloidal-silica suspension containing 5 pct hydrogen peroxide. To create high resolution large-area optical images, samples were etched in Kroll's Reagent and then image mapped with automated stage scanning using a Zeiss Axio 2 microscope. SEM electron backscatter image mapping was also conducted with an FEI Magellan field emission gun (FEG) SEM, using an accelerating voltage of 20 kV and beam current of 0.8 nA. Average  $\alpha$  inter-lamellar spacing line profiles were measured along ND using a series of 3 wide ~ 650 image tiles, acquired automatically with the FEI MAPS software, from which the average inter-lamellar spacings were calculated from each image using bespoke software that batch pre-processed the images to normalise the background before applying edge detection and utilised the linear intercept method corrected for the 2D in-plane lath angles (but not the 3D tilt).<sup>[48]</sup> The image tiles acquired had a 30 × 30 μm view field, and the inter-lamellar spacings were averaged across the wall width (in TD) and 95 pct confidence intervals were added.

EBSD and EDS maps were performed simultaneously, using a custom high-throughput Thermo Scientific Apreo C FEG-SEM, equipped with an Oxford Instruments' Symmetry 2 EBSD and Ultim MAX EDS detectors and AZtec acquisition software. The EBSD and EDS maps were acquired using an accelerating voltage of 20 kV and a beam current of 51 nA, at a pixel rate of 1800 Hz, and were processed using Oxford Instruments' Crystal software. All EBSD maps are shown in inverse pole figure (IPF) colouring with the orientation reference parallel to ND. The textures are depicted in pole figures contoured with a 10° half width and scaled in multiples of random density (MRD). Parent  $\beta$ -phase EBSD maps were reconstructed from the  $\alpha$ -phase data using the software developed by Davies and Wynne<sup>[49,50]</sup> with a maximum 2 deg disorientation from a particular  $\alpha$  variant accepted, and up to a 3 deg divergence from the BOR considered as part of the same parent  $\beta$  grain. To produce more accurate composition profiles in ND, the EDS maps were averaged in the transverse direction (TD) in the central WAAM build regions to increase the signal-to-noise ratio.



### III. RESULTS

#### A. Overview

Example optical macrographs from the Ti6242 baseline un-peened and 0.4 mm-pitch peened walls, cross sectioned in the ND-TD plane, are shown in Figures 2(a) and (b), respectively. The un-peened sample can be seen to have a coarse-columnar  $\beta$ -grain structure, similar to that found in Ti64 WAAM samples deposited with comparable process parameters,<sup>[13,22,23]</sup> with several grains visible spanning the entire field of view in ND and reaching millimetres in height. However, in the un-peened Ti6242 sample in Figure 2(a), a  $\sim 2$  mm-thick skin of much smaller  $\beta$  grains can be seen at the outer wall surfaces, which is not normally observed in Ti64 WAAM samples, but has been recently reported with a near- $\beta$  alloy, Ti5553, that also contains molybdenum.<sup>[51]</sup> Nevertheless, from Figure 2(b) it is readily apparent that, when peening is applied to the centre line of every deposited layer, the  $\beta$ -grain structure in the core of the wall has recrystallised producing refined lower-aspect-ratio grains across most of its width. The level of refinement is also similar to that previously seen for comparably peened, or rolled, single-bead Ti64 WAAM builds.<sup>[19,23,30]</sup> Since the deformation field from peening did not extend across the full TD wall thickness,<sup>[30]</sup> it should be noted that the finer recrystallised grain region does not fully reach the wall edges, although this is not immediately obvious because the unaffected near-surface regions overlap with the finer columnar 'skin-layer' visible in the un-peened sample.

The two common banding features that have been reported for WAAM Ti64 can also be seen in the optical macrographs for Ti6242 in Figures 2(a) and (b). This includes: (i) HAZ bands, seen as regular, slightly tilted, lighter lines crossing the samples in TD, which can be identified as thicker diffuse etched lines in the optical images<sup>[5,14–16]</sup>; and (ii) fainter, narrower, curved, fusion-boundary bands that arise due to transient solute partitioning during the initial acceleration of the solidification front.<sup>[5]</sup> It should also be noted that usually with WAAM single wire bead samples the HAZ bands are horizontal; but in the Ti6242 samples in Figure 2 the bands are slightly inclined due to a small misalignment error of the wall centre line relative to the heat source when the table was rotated 180 deg between each pass.

In Figure 2(c), the top of the un-peened wall is shown at a higher magnification and reveals that significant inter-dendritic solute partitioning took place during solidification of Ti6242, which is not normally visible in WAAM Ti64 optical images (*e.g.*, Reference 5). At this magnification, this is most obvious where it delineates the primary dendrite  $\langle 001 \rangle_{\beta}$  growth direction, which is approximately normal to the fusion boundary bands. This stronger etching contrast, seen at both the fusion boundaries and across the dendrites in the Ti6242 samples, compared to with Ti64, occurs because alloying elements like Mo and Si exhibit a greater deviation of their partition coefficients from unity ( $k = 2$  and  $k = 0.35$ , respectively<sup>[26,27,52]</sup>), compared to V and Al

in Ti64 where  $k$  is close to 1,<sup>[27,52,53]</sup> and thus segregate more strongly during solidification.

#### B. Grain Structure and Texture

##### 1. Primary $\beta$ -grain structure

Reconstructed  $\beta$ -phase EBSD maps of the un-peened and peened samples are compared in Figure 3, highlighted in IPF colouring relative to ND. As expected, the un-peened sample (Figure 3(a)) exhibits a very coarse columnar  $\beta$ -grain structure across its central region, with a strong  $\langle 001 \rangle_{\beta} // \text{ND}$  fibre texture (shown in Figure 4(a)), which is typical of most titanium WAAM samples built using 'standard' process parameters.<sup>[22,23,30]</sup> However, the surface skin layer of smaller grains can be seen to have a different texture. The skin grains have non- $\langle 001 \rangle_{\beta} // \text{ND}$  orientations and instead mostly exhibit  $\langle 111 \rangle_{\beta}$  and  $\langle 011 \rangle_{\beta}$  directions aligned with ND (blue and green in Figure 3), which aligns their  $\langle 001 \rangle_{\beta}$  growth direction at around  $\sim 30$  to  $50$  deg to the wall's surface. However, since the  $\langle 001 \rangle_{\beta} // \text{ND}$  fibre texture dominates the macrostructure of this undeformed sample, the texture of these refined grains is very weak in the contoured pole figure taken from the whole un-deformed wall cross section in Figure 4(a).

It can be seen from Figures 4(b) through (g) that when the inter-pass peening technique is applied, the columnar  $\beta$ -grain structures in the central wall cores were refined in all 3 samples, giving a more equiaxed structure, and the grain size decreased with reducing peening-pitch down to a minimum of  $\sim 260 \mu\text{m}$ . Additionally, with reducing peening pitch, the central recrystallised  $\beta$ -grain region widened. This is exemplified in Figure 5 where the equivalent circular-diameter grain size has been plotted across the walls in TD. Although the relative width of the refined core region is difficult to define precisely, it has been approximately indicated here from the distance between the peaks associated with the skin layer—as shown by the dashed lines in Figure 5—which gives an increase of 4.8 to 7.2 mm (+ 50 pct) when decreasing the peening pitch from 3.9 to 0.4 mm.

From Figure 4(b) it can be seen that the central region of the sample peened with the largest 3.9 mm pitch retained a relatively strong  $\langle 001 \rangle_{\beta} // \text{ND}$  fibre texture (red grains in Figure 3(b)), even though the grains were refined, giving a  $470 \mu\text{m}$  average diameter, and had a low aspect ratio. The pole figures for the full EBSD map datasets (Figures 4(a), (b), (d), (f)), and those restricted to the walls' recrystallised grain core region (Figures 4(c), (e), (g)) also show a split  $\langle 001 \rangle_{\beta} // \text{ND}$  pole fibre texture, with the most intense  $\langle 001 \rangle_{\beta}$  poles tilted towards TD by rotation around WD. The positions of greatest intensity of these split TD poles are different in the full dataset, where they can be seen to be more rotated about WD and spread out farther as the peening pitch reduces from  $\pm 30$  to  $\pm 50$  deg (Figures 4(b), (d), (f)). In comparison, the split poles in the texture data selected from the wall core regions show a smaller and more consistent deviation from ND



**Table II. Composition in Wt Pct of the Alloy Wires (As-Quoted by the Manufacturer) and of the WAAM-Deposited Ti6242 (As Measured by ICP)**

	Al	Sn	Zr	Mo	V	Si	Fe	N	O	Ti
Ti6242 Wire	6.10	2.00	4.00	2.00		0.09	0.03	0.003	0.12	bal
As-Deposited Ti6242	6.30	2.02	4.20	1.96		0.05	0.05	0.01	0.16	bal
Ti64 Wire	6.48				3.91		0.17	0.007	0.16	bal

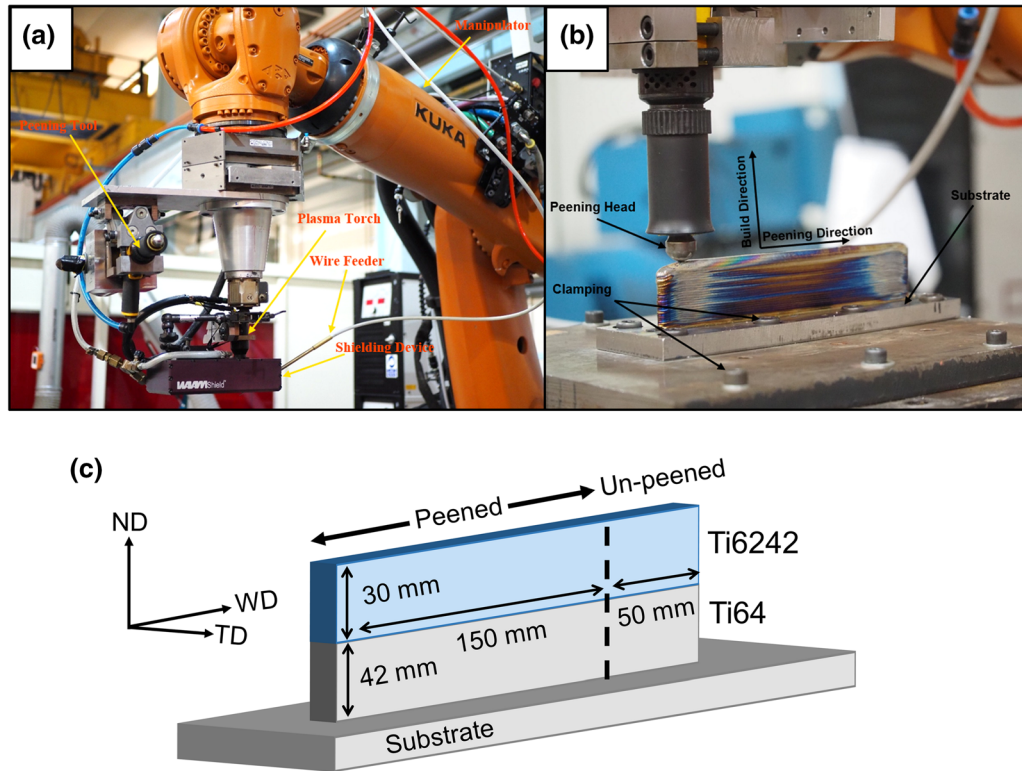


Fig. 1—(a) WAAM deposition setup, (b) inter-pass machine hammer peening setup, and (c) schematic diagram of the Ti64 → Ti6242 alloy-alloy composite wall.

with reducing peening pitch of about  $\pm 5$  deg (Figures 4(c), (e), (g)). More importantly, as the intensity of deformation increased with the reduced peening pitch, the texture progressively weakened in the refined-core grain region from  $> 14$  MRD for the non-peened baseline sample to 5.7 MRD with a 3.9 mm pitch (Figure 4(e)) and 3.3 MRD with a 0.4 mm pitch (Figure 4(g)). Finally, the observation that the wider split  $\pm 30$  to 50 deg ND intensity peaks were not seen in the reduced dataset taken only from the recrystallised wall core demonstrates that these texture components originated from the skin layer produced by solidification.

## 2. Transformation microstructures

In the un-peened Ti6242 control sample, the  $\alpha + \beta$  transformation microstructure consisted of fine ‘basketweave’ lamellar  $\alpha$  separated by very thin nanoscale retained  $\beta$  films, which is shown in the SEM micrographs in Figure 6. However, the transformation

structure differed between the top of the deposit (Figure 6(b) where the microstructure was produced by only cooling through the  $\beta$  transus ( $T_\beta$ ), to the mid-bulk of a wall (Figure 6(d)) that had also experienced several reheating cycles below  $T_\beta$ . Near the top of the wall, the as-transformed material consisted of a basketweave microstructure of fine,  $\sim 0.6 \mu\text{m}$ -thickness  $\alpha$  lamellae. A few small pockets of very fine  $\alpha$  laths (see inset in Figure 6(b)) of  $\sim 0.2 \mu\text{m}$  thickness were also found in some regions. However, after experiencing thermal cycling at temperatures below the  $\beta$  transus, the transformation structure in the lower, steady-state region of the wall had noticeably coarsened to give a slightly larger average inter-lamellar spacing of  $\sim 0.7 \mu\text{m}$ , and the much finer  $\alpha$  was no longer seen. It should be noted that the region shown in Figure 6(d) was taken avoiding the etched lines corresponding to the optically observable HAZ bands, but the transformation structure varied systematically across each layer in ND, as will be discussed farther below (Figures 7, 8). Small particles

were also found throughout the transformed  $\alpha$  microstructure, which are shown in the secondary electron micrograph in Figure 6(c). These particles were  $\sim 1 \mu\text{m}$  in size and SEM-EDS analysis revealed that they contained a significant amount of silicon, and therefore could be identified as titanium silicides.<sup>[36,44,47]</sup>

In order to quantify the heterogeneity seen in the  $\alpha$  inter-lamellae spacing throughout the full Ti6242

WAAM build, large SEM backscatter image tile maps (Section II-B) were automatically acquired along the build direction, up the wall centre line, and batch analysed using bespoke software.<sup>[48]</sup> A plot of the average (2D) inter-lamellar spacing measured by this method, with build height, is shown for the un-peened sample in Figure 7 from the area highlighted in the optical macrograph. For the bulk of the wall, the inter-lamellar spacing in Figure 7 exhibited a ‘sawtooth’ wave profile with a pitch equivalent to the layer height. At the top of the wall ( $> 16 \text{ mm}$  in Figure 7), for the last 4 layers, where the material was fully reheated into the  $\beta$ -phase field during each pass of the heat source and only transformed during cooling, the  $\alpha$  inter-lamellar spacing showed no systematic variance across the added layers (other than from systematic noise). The sawtooth wave pattern seen in the bulk, and the lack thereof in the fully  $\beta$ -annealed top of the wall, are very similar to the behaviour reported formerly for similar Ti64 WAAM builds, which is discussed at length in Reference 5. It can also be noted that in the older Ti64 WAAM build analysed previously, there was a gradual increase in  $\alpha$  inter-lamellar spacing towards the bottom of the wall due to the heat accumulation experienced during deposition, which was a result of the build temperature not being actively monitored and used to control the heat-source return time. In comparison to the current work, the build inter-pass top surface temperature was kept considerably lower and constant at  $100 \text{ }^\circ\text{C}$ , such that no long-range microstructure coarsening was observed. Nevertheless, from the data in Figure 7 it is still evident that the whole steady-state lower part of the wall, where the HAZ band sawtooth wave pattern is seen, had a coarser  $\alpha$  lamellar spacing on average than the top  $\sim 4$  layers of the build that did not experience reheating below  $T_\beta$ , after cooling from the  $\beta$  phase field.

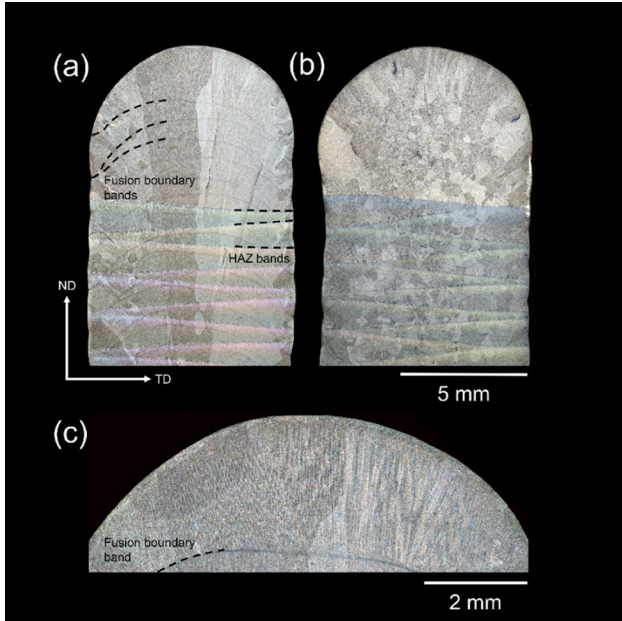


Fig. 2—Optical macrographs of WAAM Ti6242 walls showing top ND-TD sections from (a) the un-peened control sample and (b) the sample peened with a 0.4 mm pitch. (c) shows the top of (a) at higher magnification. Typical WAAM microstructural banding features have been highlighted in (a).

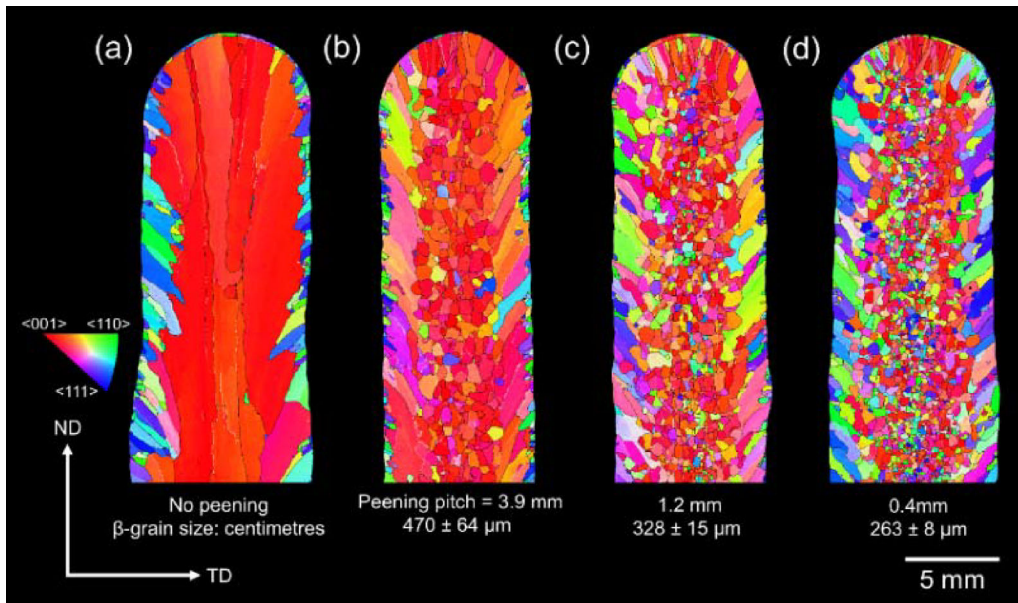


Fig. 3—Reconstructed  $\beta$ -phase EBSD maps of the 4 Ti6242 WAAM test builds showing: (a) the un-peened control sample, and builds produced where the top surface of each layer was peened with pitches of (b) 3.9 mm, (c) 1.2 mm, and (d) 0.4 mm. All maps are shown in IPF colouring relative to the normal (build) direction (ND) (Color figure online).

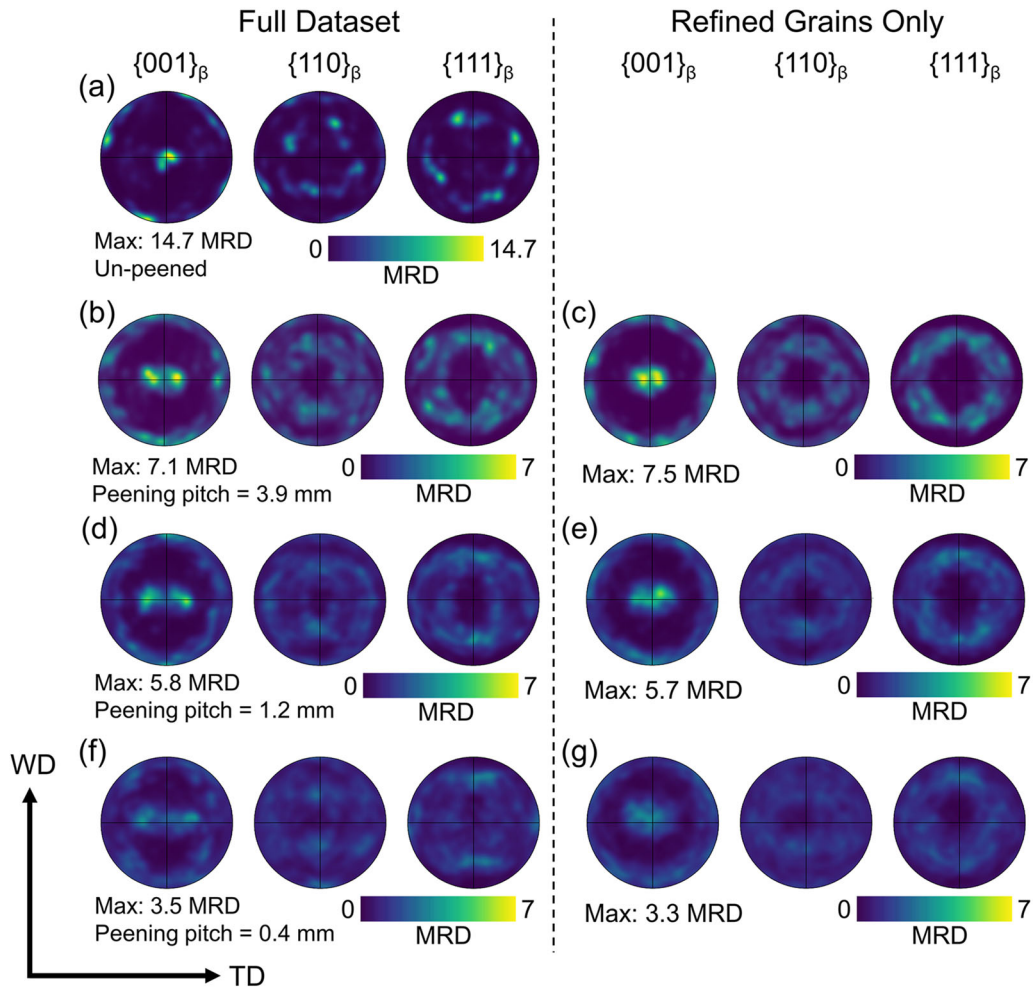


Fig. 4—Pole figures showing textures obtained for the  $\beta$  phase, from the full reconstructed EBSD maps in Fig. 3 of (a, b, d, f) the full datasets and (c, e, g) only from the recrystallised wall core grain regions produced by peening. (a) shows the un-peened sample's texture, and (b) and (c), (d) and (e), (f) and (g) show the textures of the samples peened with pitches of 3.9, 1.2, and 0.4 mm, respectively. Note: the contour intensity of (a) is scaled differently to that of (b) and (g).

The first two top HAZ bands of the Ti6242 inter-lamellar spacing sawtooth wave pattern (highlighted in Figure 7) are magnified in Figure 8(a), to show the coarsening behaviour of the  $\alpha$  laths in more detail. Example SEM backscatter electron micrographs are also supplied in Figure 8 from regions of interest where: (b) depicts the material at the top of the wall, where it was fully transformed to  $\beta$  during reheating and cooled without subsequent sub-transus reheating; (c) is from reheating high in the  $\beta$  approach curve, where the  $\alpha$  lamellae have coarsened and the inter-lamellar spacing is greatest ( $\sim 0.8 \mu\text{m}$ ); and (d) gives an example of the fine-scale lamellae (inter-lamellar spacing  $\sim 0.6 \mu\text{m}$ ) associated with the thin sublayer of single-variant  $\alpha$  colonies formed at the top of the HAZ bands. This latter microstructure is nearly identical to the  $\alpha$  colony 'packet' structure reported in Reference 5 at the same position for Ti64. These features have all been labelled in Figure 8.

### C. Direct Comparison to Ti-6Al-4V

Ti64 has dominated previous research for metal DED AM processes with titanium, such as WAAM (e.g., Reference 13, 18–21), and is still the most popular choice for many aerospace applications, therefore it is of significant interest to make a direct comparison between the Ti64 and Ti6242 WAAM microstructures. Here, to ensure the deposition conditions used for Ti6242 exactly matched those for Ti64, a larger WAAM test wall was built that included layers of the two alloys, without altering the process parameters, by changing the alloy wire feed midway through deposition; thereby, creating a composite alloy sample for examination, where each alloy experienced an *identical* process history. Inter-pass peening with a pitch of 0.4 mm was also again performed to refine the grain structure in both alloy regions, but across only three quarters of *each* added layer, so that cross-sections could be extracted from regions with either coarse-columnar or refined  $\beta$  grains



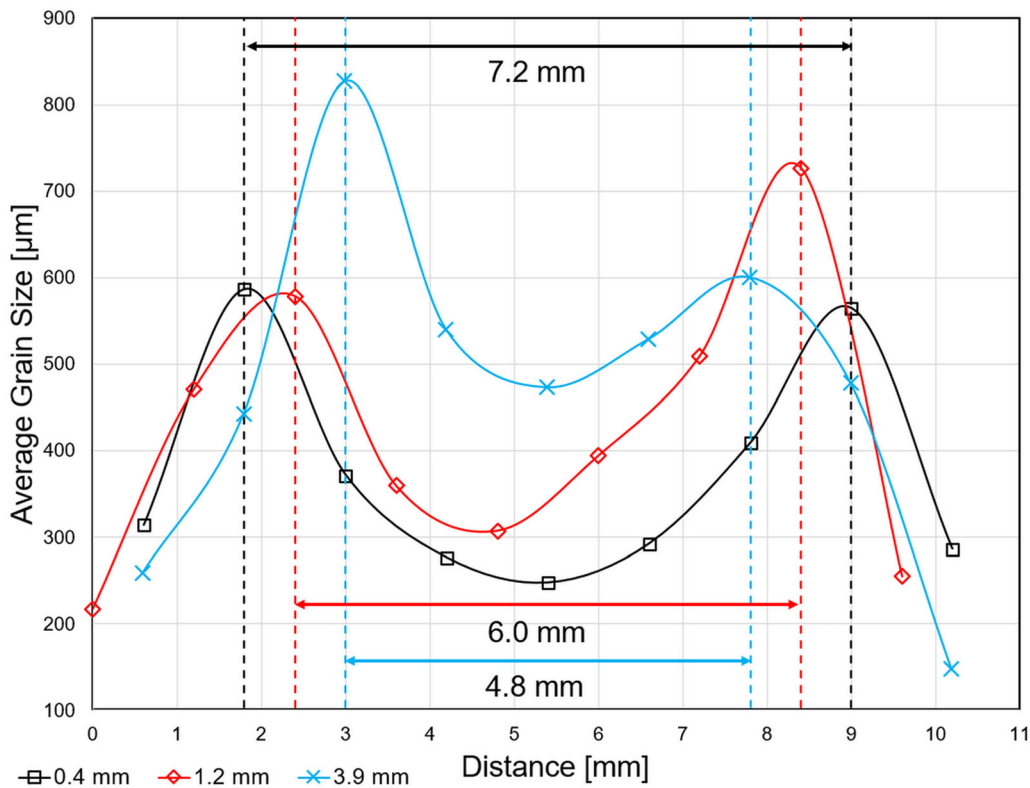


Fig. 5—Average  $\beta$ -grain size (equivalent circular diameter) profiles measured across the peened wall samples in TD, for different peening pitches (0.4, 1.2, 3.9 mm) taken from the EBSD maps in Fig. 3b through d. The central grain-refined region for each peening pitch is highlighted by the dashed vertical lines. The grain size data was binned for every 200  $\mu\text{m}$  in TD.

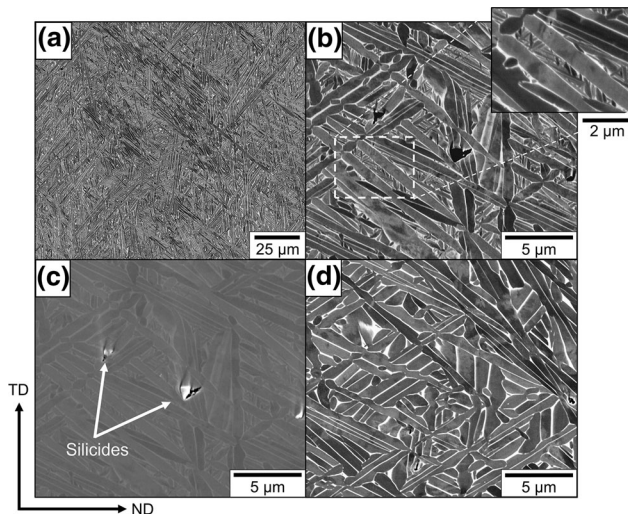


Fig. 6—SEM micrographs showing the un-peened Ti6242 control sample's typical transformation microstructure at (a) low and (b) and (c) high magnifications. The inset shows the very fine, secondary  $\alpha$  laths, taken seen in the top of the wall that had transformed by only cooling from above the  $\beta$  transus (*i.e.*, without reheating below  $T_{\beta}$ ). (d) shows the typical bulk microstructure from the midpoint of the wall height (between the HAZ bands). (a, b, d) were obtained using the backscatter electron camera and (c) was taken with the secondary electron camera to reveal the titanium silicide particles more clearly (identified using EDS point analysis).

(a schematic is provided in Figure 1(c)). In addition, this AAC sample was also used for determining the extent of chemical mixing and the microstructure gradient that will occur across a dissimilar alloy transition when manufacturing property-tailored parts. An optical macrograph of the alloy-alloy transition in the un-peened region of the wall is provided in Figure 9(a) and shows the typical WAAM HAZ banding features continue across both alloys with a regular spacing. Unlike for the monolithic Ti6242 samples in Figure 2, the heat source was better centred during alternating the travel direction with this build so that the HAZ bands are more parallel and not inclined when cross sectioned in ND-TD. Thinner fusion boundary bands can also again be seen but, due to the difference in partition coefficients of the main elements in the two alloys and their respective etching responses, they are only visible in the upper Ti6242 section<sup>[26,27,51]</sup>. Large columnar  $\beta$  grains are also again visible that grow unhindered across both materials and through the alloy-alloy interface.

The extent of chemical mixing across the dissimilar alloy transition was studied using SEM-EDS and the composition gradients are shown in Figure 9(b). When the feed wire is changed in the WAAM process, the alloy transition regions are known to exhibit a stepwise composition gradient that spans several layers.<sup>[51]</sup> This is caused by the  $\sim 50$  pct dilution that occurs of each new layer due to the high remelt depth, which is combined with effective convective liquid-phase

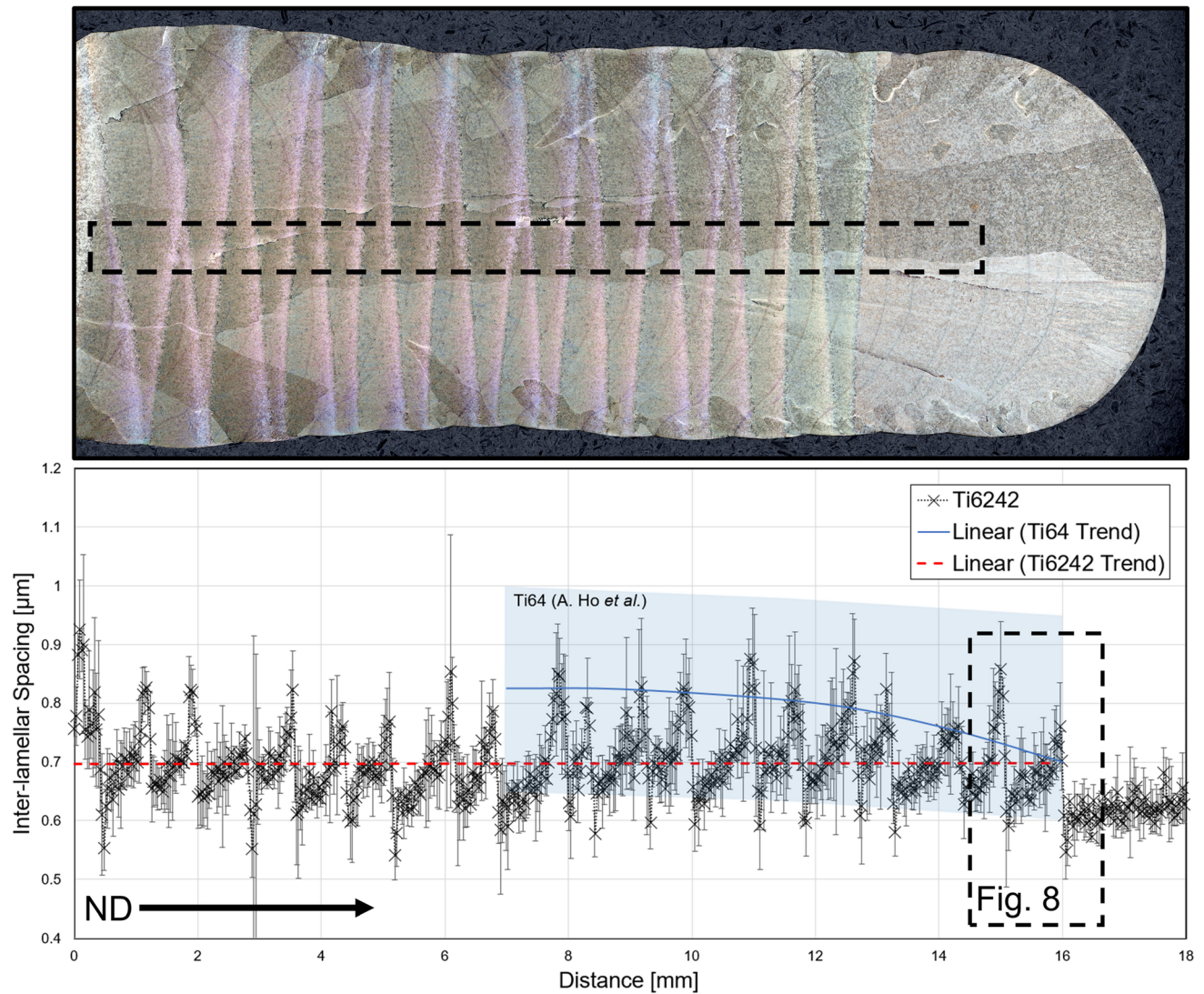


Fig. 7— $z$  inter-lamellar spacing line profile of the un-peened Ti6242 sample in the build-height direction (ND) taken from the region highlighted at the top optical macrograph. A linear trend line has been added to the data in red. Additionally, the inter-lamellar spacing trend from a Ti64 WAAM sample (blue line) has been included for comparison (data taken from Ref. [5]), where the shaded region indicates the approximate maximum and minimum spacing values (Color figure online).

mixing.<sup>[51]</sup> When transitioning from Ti64  $\rightarrow$  Ti6242 (in ND), there is an immediate large increase in the EDS count intensities for Mo, Si, Sn, and Zr, due to the change in wire composition (the photon counts before the transition region are background noise). However, the nominal composition of Ti6242 is not approached until  $\sim 4$  mm after the alloy wire was switched, which is equivalent to adding  $\sim 4$  more deposited layers. In the inter-mixing region, compositional ‘ledges’ can be seen, similar in appearance to reported previously,<sup>[51]</sup> that correspond to each new added layer of Ti6242, with a steep transition gradient at each fusion boundary that builds up a ‘stepwise’ exponential dilution profile. Within each ‘step’ some localised composition variation can also be noted (particularly in Mo, Sn, and Zr) that is a consequence of incomplete mixing in the melt pool.<sup>[54]</sup> In addition, transient solute partitioning away from the fusion boundary layers can clearly be observed for Si,

which has a low partition coefficient ( $k = 0.35$ <sup>[52,53]</sup>) and Zr ( $k = 0.86$ <sup>[52,53]</sup>), once the nominal Ti6242 composition has been reached ( $> 9$  mm in Figure 9(b)). More modest transient fusion boundary partitioning of Al, V, and Fe has also been previously detected in Ti64 using electron probe microanalysis, but EDS lacks the elemental sensitivity to resolve this low level of partitioning.<sup>[5]</sup>

An SEM backscatter electron image-tile map was acquired of the Ti64  $\rightarrow$  Ti6242 build along the centre line with height (ND), so that the average inter-lamellar spacings of both alloys could be measured and compared. This line profile is shown in Figure 9(c) along with the zirconium EDS signal so it can be correlated to the alloy-alloy transition mixing region. The typical transformation microstructures observed for both alloys are also shown in Figure 10. As expected from the HAZ bands present, the same inter-lamellar spacing sawtooth



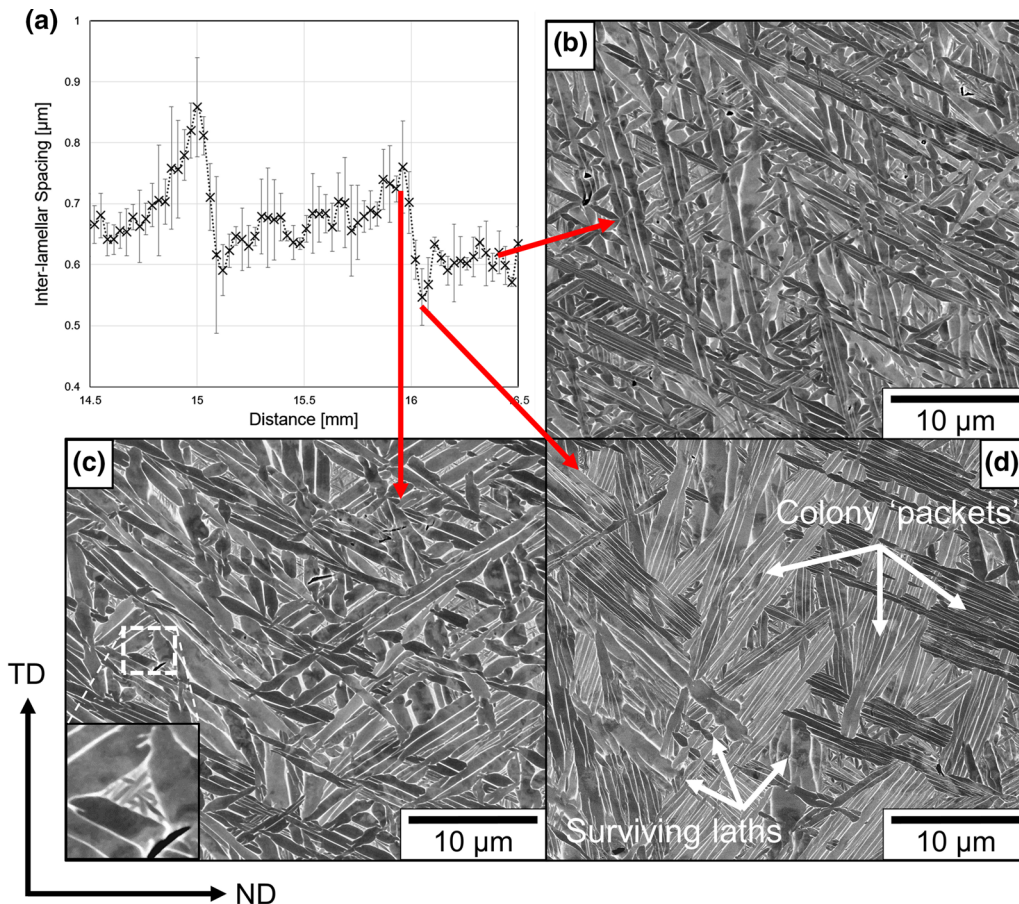


Fig. 8—(a) Magnified average  $\alpha$  inter-lamellar spacing line profile taken from the region below the last HAZ band highlighted in Fig. 7 in the control un-peened Ti6242 build; accompanied by example SEM backscatter electron images of the (b)  $\alpha + \beta$  microstructure taken from the wall top (only reheated above the  $\beta$  transus during deposition), (c) the coarsened microstructure from the  $\alpha \rightarrow \beta$  partially retransformed area of the HAZ band, and (d) the colony ‘packet’ transformation structure that results from being reheated just below the  $\beta$  transus.

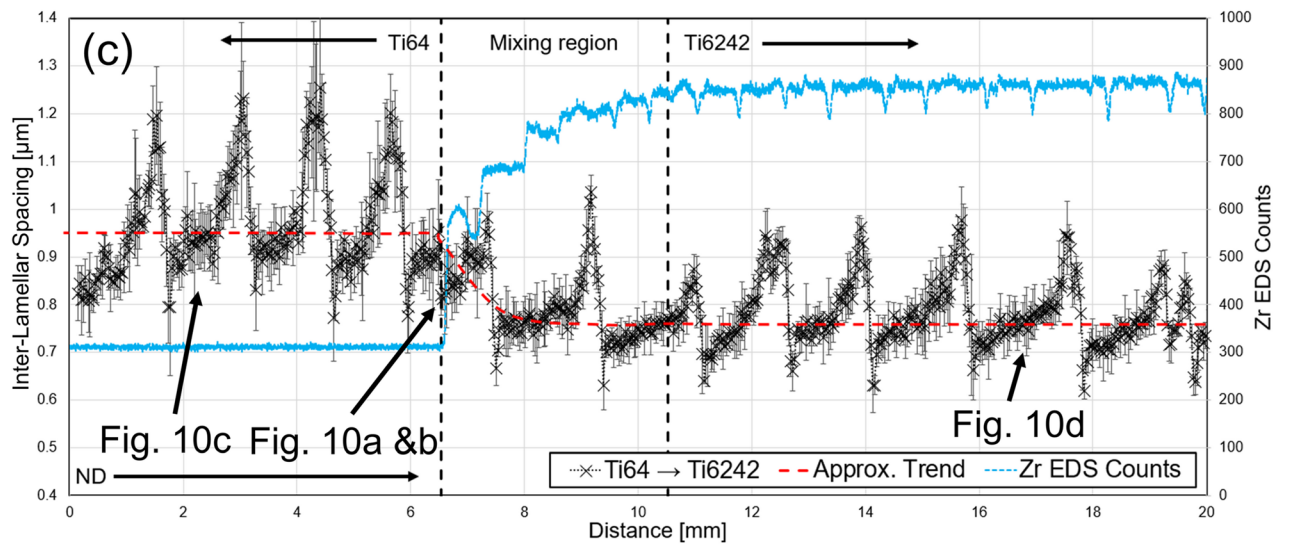
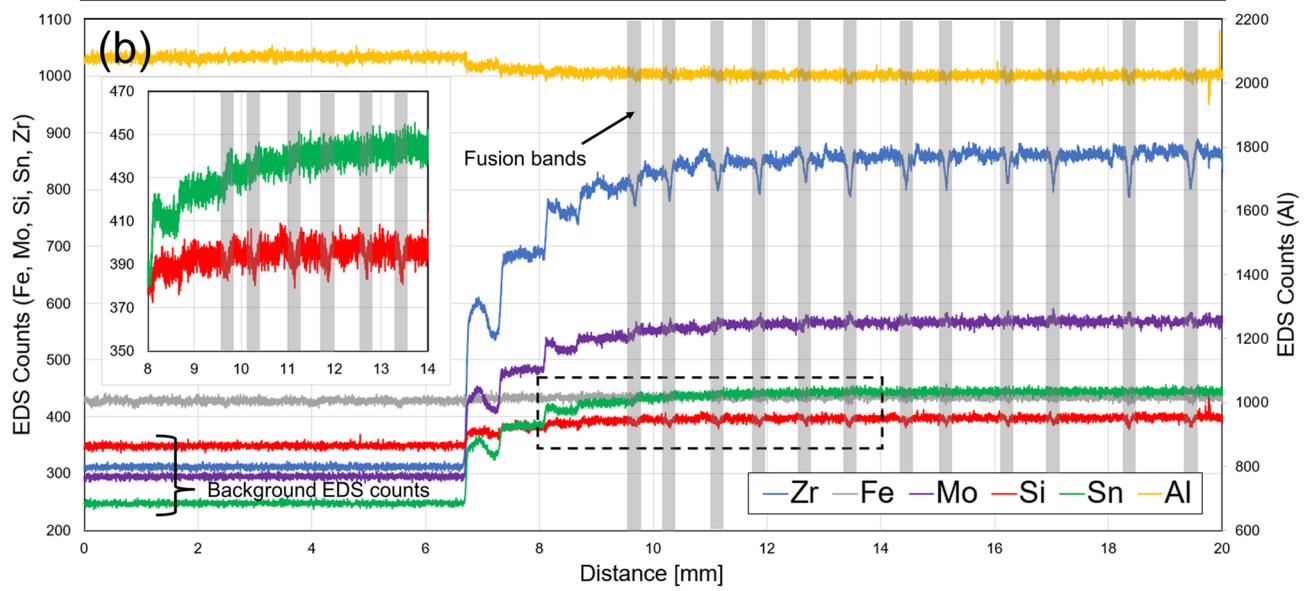
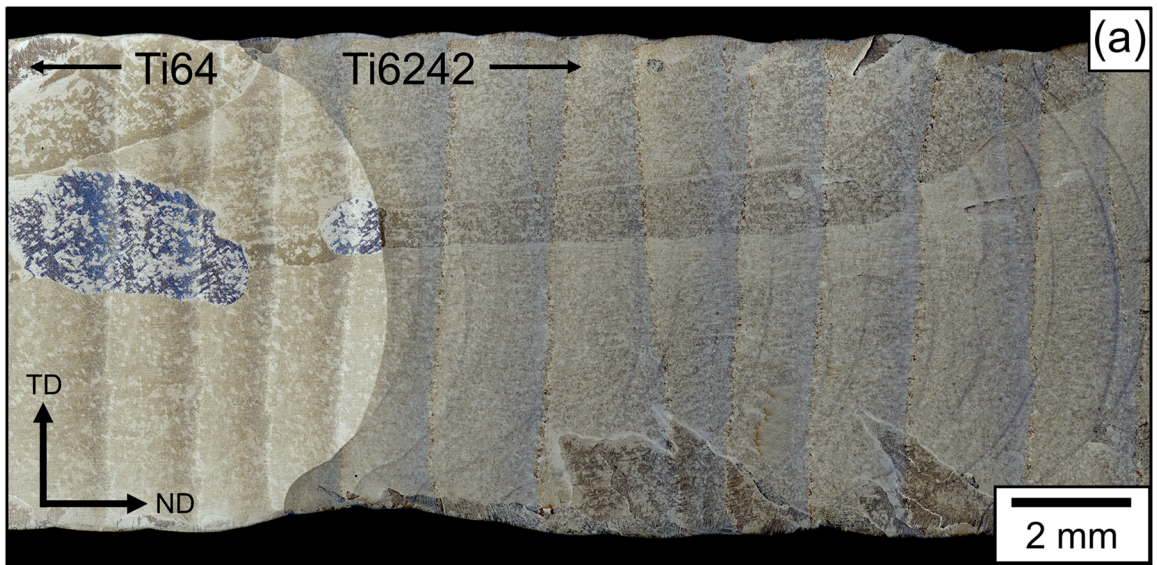
wave pattern was found throughout both alloys, noted above. However, when the alloy feed-wire was switched to Ti6242 ( $> 6$  mm in Figure 9(c)), there was first a gradual reduction in the overall inter-lamellar spacing (0.8 to 1.4  $\mu\text{m} \rightarrow 0.6$  to 1.0  $\mu\text{m}$ ), until a new steady state was again achieved once the nominal composition of Ti6242 was reached ( $> 10$  mm), which is exemplified by the trend line in Figure 9(c); *i.e.*, when deposited under identical conditions, Ti6242 had an  $\alpha$  lamellar spacing finer than that of Ti64. Finally, it should be noted that the average inter-lamellar spacing of the Ti6242 section of the AAC deposit was slightly coarser than that of the monolithic un-peened Ti6242 sample shown in Figure 7. This is probably due to the higher inter-pass temperature used (200 °C) with this build that will have resulted in lower cooling rates and thus a coarser initial  $\alpha + \beta$  microstructure.<sup>[36,55,56]</sup>

A  $\beta$ -reconstructed EBSD map in the peened section of the same Ti64  $\rightarrow$  Ti6242 AAC build is also shown in Figure 11(a), and the  $\alpha$  and  $\beta$  textures for each alloy are provided in the pole figures in Figure 12. Similar to the 0.4 mm-pitch peened monolithic Ti6242 sample in Figure 3(d), the centre region of the TD-ND cross section has been successfully refined into weakly

Fig. 9—Microstructural and compositional analysis data obtained across the transition in the Ti64  $\rightarrow$  Ti6242 alloy-alloy composite sample: (a) optical macrograph of the etched transition region, (b) high-resolution EDS photon-count line scans across the sample length (averaged across the central TD section) with an insert magnifying the region indicated by the black dotted rectangle, (c) the average  $\alpha$  inter-lamellar spacing profile measured by automated image mapping down the sample centreline, accompanied by the Zr EDS signal so that it can be correlated to the region of alloy-alloy mixing.

textured, near-equiaxed  $\beta$  grains in both the Ti64 and Ti6242 wall sections and across the alloy-alloy transition. However, analogous to the behaviour of the  $\alpha$  inter-lamellar spacing, there is a reduction in the  $\beta$ -grain size once the deposition wire was switched to Ti6242. This is exemplified in Figure 11(b), where the grain size averaged every 200  $\mu\text{m}$  is again plotted alongside the zirconium EDS signal to identify the location of the alloy-alloy transition region. The average trend line shows there is a  $\sim 25$  pct reduction in the  $\beta$ -grain size relative to that of Ti64 across the region of intermixing to the Ti6242 section of the sample. Although the Ti6242 layers of the AAC wall exhibited a smaller grain





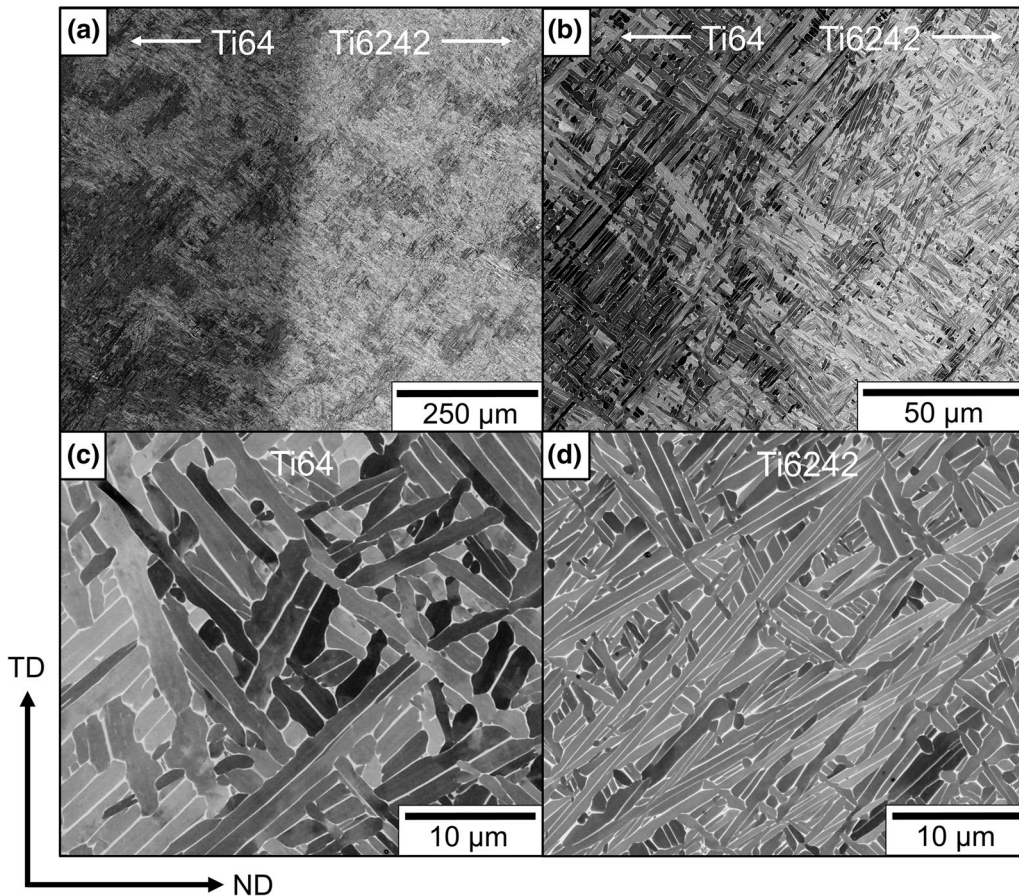


Fig. 10—SEM backscatter electron micrographs of the Ti64 → Ti6242 alloy-alloy composite sample showing the transformation microstructure in the interface between the Ti64 and the first deposited layer of Ti6242 at (a) low and (b) higher magnification, and in (c) the Ti64 and (d) the Ti6242 bulk  $\alpha + \beta$  microstructures.

size, the  $\beta$ -phase textures of the Ti6242 and Ti64 shown in Figures 12(a) through (d) were comparably weak (both  $\sim 3$  MRD in the peened recrystallised core grain region dataset and  $\sim 4$  MRD for the entire wall section) and again exhibited the split  $\langle 001 \rangle_{\beta} // \text{ND}$  pole fibre texture. The  $\alpha$  texture was also diluted further during the  $\beta \rightarrow \alpha$  phase transformation such that is close to random, as can be seen in Figures 12(e) and (h).

#### IV. DISCUSSION

Although this study was performed on simple linear single-track-wide test samples, with a single peening pass applied across the top surface along each wall centre line, the application of an increasing energy density with inter-pass peening has been shown to lead to the formation of a greatly improved  $\beta$ -grain structure and weaker texture in a Ti6242 alloy after deposition by the WAAM process. Under the same conditions, the level of grain refinement achieved was also greater than that previously obtained with the more commonly studied alloy Ti64.<sup>[19,30]</sup> In the Ti64 → Ti6242 alloy-alloy composite sample (Figure 11), the overall grain size and scale of the transformation microstructure were also both found to be approximately 25 pct finer in the

Ti6242 alloy, compared to Ti64, and the extent of  $\beta$ -grain refinement produced by peening transitioned smoothly across the interface region. Very similar transformation basketweave microstructures and HAZ banding features were also seen in both alloys.

Ti64 and Ti6242 have only a relatively small difference in their  $\beta$ -phase stability and the alloys also have similar  $\beta$ -transus temperatures of  $\sim 980$  °C<sup>[5,57]</sup> and  $\sim 995$  °C,<sup>[36,42]</sup> respectively. However, Ti6242 is alloyed with molybdenum, which has a much slower solid-state diffusivity than vanadium, the slowest diffusing species in Ti64.<sup>[26]</sup> When compared to Ti64, this difference in diffusivity is known to impede the  $\beta$ -grain growth kinetics,<sup>[56,58,59]</sup> and the growth rate of  $\alpha$  laths during the  $\beta \rightarrow \alpha$  transformation<sup>[60]</sup>; so it is perhaps not surprising that Ti6242 was found to have an overall more refined microstructure. Given that both materials were built with near-identical thermal histories, with multiple-heating cycles above and below the  $\beta$  transus, where the  $\beta$  grains and  $\alpha + \beta$  transformation microstructure have ample opportunity to coarsen, the results demonstrate that the presence of slower-diffusing alloying additions in titanium alloys like Ti6242 appear to be advantageous for refining the as-deposited microstructure in a high-deposition-rate AM process, which have higher heat inputs and lower cooling rates



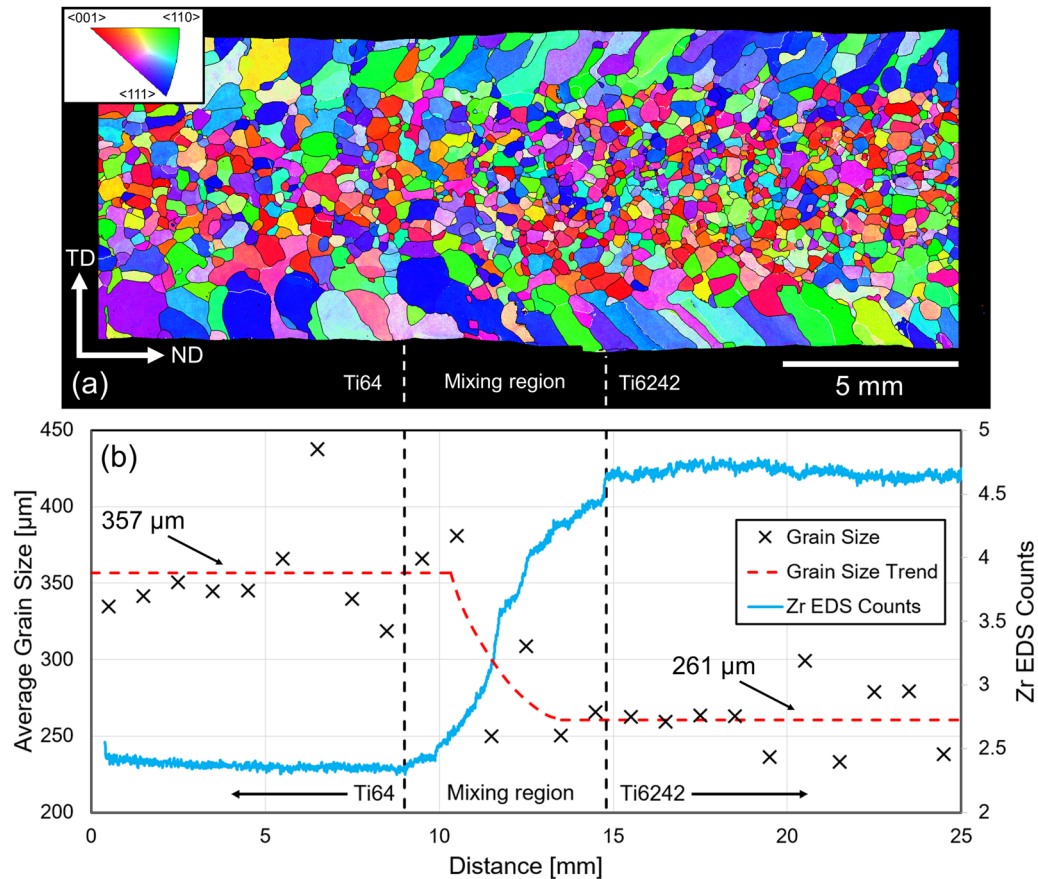


Fig. 11—EBSD analysis of the  $\beta$ -grain structure in the Ti64  $\rightarrow$  Ti6242 alloy-alloy composite sample: (a)  $\beta$ -reconstructed EBSD maps for the two alloys with the transition region highlighted, (b) the average  $\beta$ -grain size (equivalent circular diameter) plotted against distance in the build-height direction (ND) where the data was binned across TD every 200  $\mu\text{m}$ . The trend line was drawn manually to guide the eye. A low-resolution zirconium EDS line scan (averaged across the full TD width) is also included to indicate when the wire feed was switched to the Ti6242 alloy during deposition.

than more conventional AM platforms, such as powder bed.

#### A. $\beta$ -Grain Refinement and Texture

Previous stop action studies have shown in the WAAM process with inter-pass peening that  $\beta$  recrystallisation occurs during rapid heating through the  $\alpha \rightarrow \beta$  transformation.<sup>[30]</sup> Since the heating rate is  $\sim 600 \text{ }^\circ\text{C s}^{-1}$ ,<sup>[29]</sup> the exact mechanism could not be easily studied directly with current techniques. However, in previous studies of Ti64 WAAM using inter-pass rolling, similar but greater  $\beta$ -grain refinement was achieved than by peening. This was found to give a finer equiaxed grain structure of  $\sim 140 \text{ }\mu\text{m}$ , after applying surprisingly small plastic strains of  $\sim 9$  pct.<sup>[17,23,30]</sup> Similar recrystallised grain structures were also replicated in plane-strain-compressed samples that were heated, at a high heating rate to above the  $\beta$  transus, to reproduce the WAAM thermal conditions.<sup>[56]</sup> By simulating the WAAM thermal cycle in a thermal-mechanical simulator, in a sample with a temperature gradient across  $T_\beta$ , so that the sample bulk was heated above the  $\beta$  transus to induce recrystallisation and the sample edges remained below, to retain the original

deformed parent columnar grains, the recrystallised grains were identified as having an unusual 4 pole motif texture that was related to the orientations of their parent  $\beta$  grains.<sup>[29]</sup> It was consequently shown that the recrystallisation mechanism under these conditions was consistent with the formation of new, strain-free  $\beta$  grains by defects in the  $\alpha/\beta$  interface, introduced during cold deformation, promoting annealing twinning during the  $\alpha \rightarrow \beta$  transformation when rapidly reheating a fine, deformed lamellar AM microstructure above the  $\beta$  transus. Other sources of recrystallisation nuclei were also seen in plane-strain-compressed samples at locations of high plastic heterogeneity, such as  $\alpha$  colony boundaries and within deformation bands.<sup>[56,61]</sup> A similar behaviour is thus inferred here, although a comparable study has not yet been repeated to determine if the higher strain rate and more complex strain field generated by the peening process provides a different source of new  $\beta$ -grain orientations when the  $\beta$  phase regrows during the transformation, such as from shear bands, which would make an interesting follow-on study.

The EBSD maps of the Ti6242 peened samples (Figure 3) showed that, with decreasing peening pitch, the  $\beta$ -grain size in the recrystallised regions in the walls'



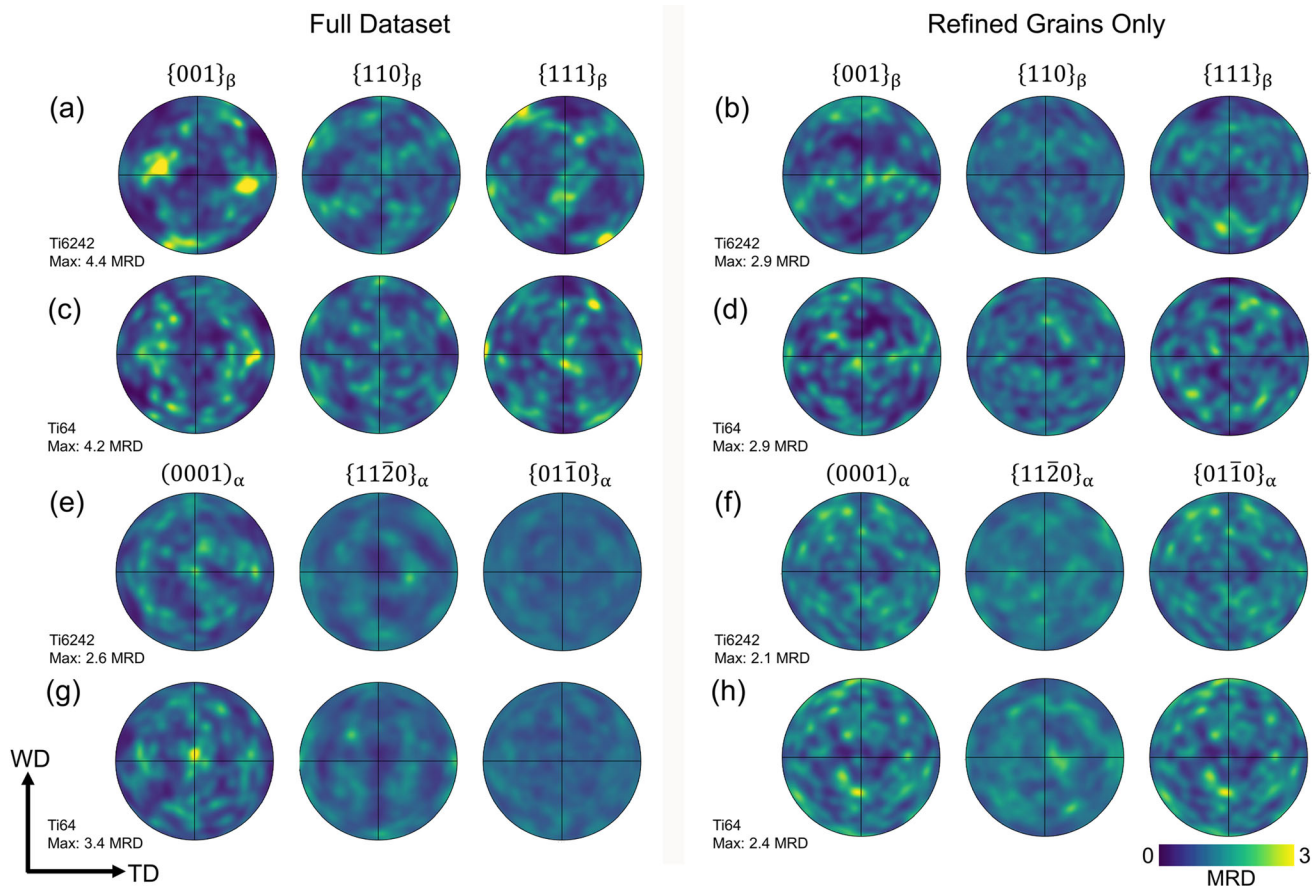


Fig. 12—Pole figures displaying the texture of the peened Ti64 → Ti6242 composite sample (Fig. 11): (a) through (d) reconstructed  $\beta$  phase and (e) through (h)  $\alpha$  phase of the Ti6242 and Ti64 segments, respectively; where (a, c, e, g) show the full texture datasets and (b, d, f, h) show reduced datasets from the recrystallised wall core grain regions produced by peening.

cores was reduced from 470 to 263  $\mu\text{m}$ , which was also accompanied by a significant reduction in the  $\beta$  texture strength from  $\sim 14$  for the un-peened control sample to only 3.5 MRD with the smallest peening pitch (Figure 4). Following transformation, the  $\alpha$  texture was further weakened by the 12 possible variants it can potentially adopt from each parent grain by the BOR, which gave rise to a near-random bulk  $\alpha$  texture in the final material deformed with the highest energy density (Figures 12(e) through (h)). It has been shown previously<sup>[56]</sup> that increasing the plastic strain produces a reduction in  $\beta$ -grain size, but the level of refinement is also strongly affected by grain growth during reheating above  $T_\beta$ , which will tend to normalise the grain size distribution. No specific grain-growth studies have yet been conducted after inter-pass machine hammer peening, but it seems reasonable to assume that the reduction in peening pitch and a corresponding increase in energy density would cause more overlap of the strain fields from each peening position, as well as increase the overall magnitude of cold work within the surface-deformed layer. This would thus be expected to have a similar effect to increasing the load in inter-pass rolling<sup>[17,23]</sup> and produce more grain nuclei that are more uniformly distributed in the peened samples, and a finer recrystallised grain size even after grain growth above  $T_\beta$ .

A previous study used ‘stop-action’ experiments to investigate the recrystallisation process in WAAM Ti64 samples with inter-pass peening.<sup>[30]</sup> Although this work used a different peening tool and energy density, it has shown that the depth of deformation below the top surface, where new grain orientations are produced, is typically less than the remelt depth with peening. However, the new recrystallised grains were still found to survive remelting by recrystallising and growing downwards ahead of the melt pool as the heat source approached.<sup>[30]</sup> These recrystallised  $\beta$  grains that were partially melted back, but survived the passage of the heat source, then became the fusion boundary and provided the ‘seed grains’ that regrew upwards, epitaxially, during solidification at the rear of the translated melt pool. Although these grains had a weak texture initially after recrystallisation, during their regrowth,  $\langle 001 \rangle_\beta$  orientated grains that were preferentially aligned with the steepest thermal gradient at the solidification front grew more quickly and overgrew grains of other orientations, and a  $\langle 001 \rangle_\beta$  fibre texture re-emerged towards the top of the newly added layer. This situation will have been exacerbated if there were fewer new seed grains in each added layer—*i.e.*, if there was a larger peening pitch and less strain-field overlap—as some grains may then have also survived across several added

layers as there will be less competition from new non- $\langle 001 \rangle_{\beta}$  // ND grains, leading to a larger grain size and preservation of a weakened  $\langle 001 \rangle_{\beta}$  // ND fibre texture.

This effect could readily explain the texture weakening and grain-size reduction exhibited by the peened Ti6242 samples seen in this work (Figures 3 and 4) with decreasing peening pitch. For example, decreasing the pitch from 3.9 to 0.4 mm produced a reduction in both  $\beta$ -grain size (470 to 263  $\mu\text{m}$ ) and texture strength (7.1 to 3.5 MRD), due to more new randomly orientated recrystallised grains surviving remelting in each added layer within the wall core.

However, split  $\pm 5$  to 10 deg TD,  $\langle 001 \rangle_{\beta}$  // ND fibre textures were seen in the recrystallised wall cores of the peened samples, which were strongest in the sample produced with the largest pitch, despite it having a finer recrystallised grain structure than the un-peened control sample (Figures 3 and 4). One possibility is that the split pole could occur because the new refined grains were mainly only able to grow within 1 added layer, rather than across multiple layers like in the baseline sample. Thus, because the build was rotated by 180 deg between each pass to reverse the heat source travel direction in each alternate layer, with a heat source that had a slight misalignment, a corresponding alternating tilt in the melt pool surface across TD may be being reflected in a corresponding small alternating deviation angle in the preferred growth direction of the new grains formed in each added layer. For example, the deviation angle from ND of the split poles in the pole figures obtained from the core of the wall (Figures 4(c), (e), (g)) is similar to that of the  $\pm 5$  to 10 deg tilt seen in the alternate HAZ bands in Figure 2. However, this effect would then manifest itself in the grains from each alternate layer showing a systematic alternating  $\pm 5$  to 10 tilt, which is not observed in the additional figure in Figure 13, where grains from each split pole have been separated in the EBSD map. Alternatively, the  $\pm 5$  to 10 deg split poles seen in the wall core could be produced by the convex curvature of the melt pool base, which will be returned to further below.

In the Ti64 and Ti6242 inter-pass peened AAC sample (Figure 11), there was a  $\sim 25$  pct reduction of the  $\beta$ -grain size across the alloy-alloy transition gradient region from the Ti64 to the Ti6242 section (357 and 261  $\mu\text{m}$ , respectively). There are two potential sources of this disparity: (i) a possible difference in the density of recrystallised nuclei between the two alloys, and (ii) the known impact of molybdenum in Ti6242 on diffusion-controlled  $\beta$ -grain coarsening in titanium<sup>[56,58,59]</sup> during thermal cycling above  $T_{\beta}$ . The coarsening kinetics of  $\beta$  grains in Ti64 in the inter-pass rolling WAAM process have been previously studied by the current authors using experimental thermal simulations,<sup>[56]</sup> but no such investigation has yet been published for WAAM Ti6242, nor to the authors' knowledge for grain growth rates in conventional wrought Ti6242 samples. Nevertheless, it is well known that solute can exert a drag pressure and control boundary mobility during grain growth. The potency of the drag is

dependent on the level of grain boundary segregation and the solid-state solute diffusivity, which is exemplified by theoretical models such as the Cahn-Lücke-S-tüwe (CLS) impurity drag model.<sup>[62,63]</sup> For example, at 1300 °C, vanadium, the slowest species in Ti64, diffuses 2.5 times faster than molybdenum in Ti6242.<sup>[64]</sup> Therefore, alloys like Ti6242 that contain much slower diffusing solute than Ti64, would be expected to give rise to a smaller  $\beta$ -grain size after thermal cycling above  $T_{\beta}$ , irrespective of the recrystallisation mechanism if the final grain size is dominated by grain coarsening.

Our previous WAAM Ti64 inter-pass peening stop-action study<sup>[30]</sup> showed this is likely to be the case, as the  $\beta$ -grain size initially formed by recrystallisation during the  $\alpha \rightarrow \beta$  transformation (*i.e.*, just above  $T_{\beta}$ ) after peening was  $\sim 20 \mu\text{m}$ , and due to the high temperatures reached by reheating in the  $\beta$  phase field, this was 5 to 10 times smaller than that seen in the final build. In addition, in a further prior study by the current authors<sup>[56]</sup> using plane-strain-compressed and rapidly

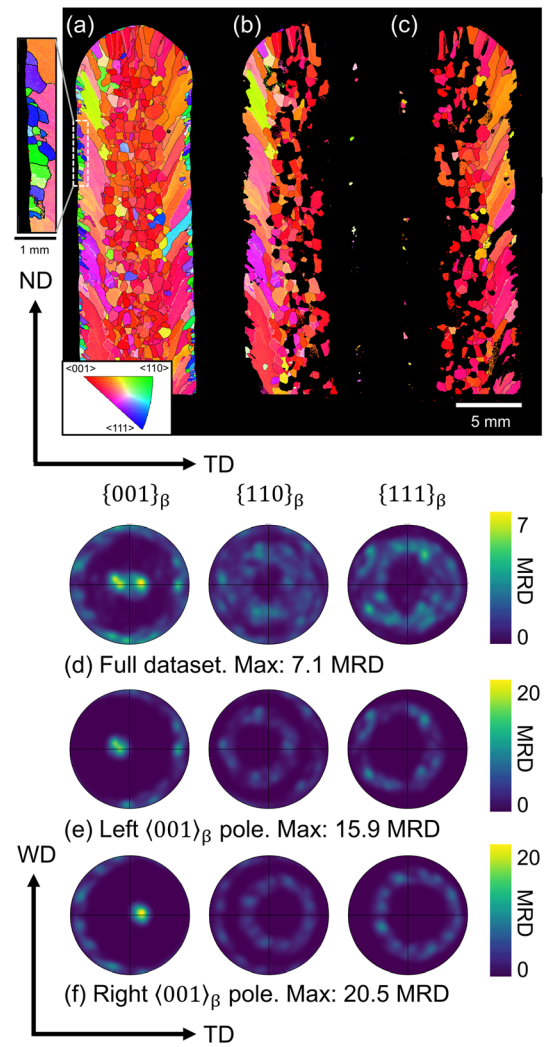


Fig. 13— $\beta$ -reconstructed EBSD maps and pole figures of the 3.9 mm-pitched peened sample where the full dataset (a, d) has been split by separating out the grains represented by the left (b, e) and right (c, f)  $\langle 001 \rangle_{\beta}$  // ND texture poles.



heated Ti64 WAAM samples, the  $\beta$ -grain growth rate above  $T_\beta$  was measured, and fitted to a conventional grain-coarsening law (e.g., Reference 59). This was subsequently used to demonstrate that a single reheating cycle of the deformed WAAM microstructure close to the melting temperature (i.e., the WAAM fusion boundary during subsequent wire layer deposition) would result in an increase of the initially recrystallised grains from 20 to 320  $\mu\text{m}$ . Subsequent heating cycles occur as more layers are added, which have a rapidly reducing peak temperature, and were predicted by the model to contribute to little further grain growth. This prediction is thus consistent with the experimentally measured value of the Ti64 in this work (357  $\mu\text{m}$ ). Unfortunately, a similar  $\beta$ -grain growth experimental dataset and model do not currently exist for Ti6242 and will be the subject of a following publication.

It is further interesting that all the Ti6242 samples—both peened and un-peened—exhibited an outer skin layer of smaller columnar  $\beta$ -grains, that predominantly had  $\langle 110 \rangle_\beta$  and  $\langle 111 \rangle_\beta // \text{ND}$  orientations (green and blue, Figure 3). This skin layer has not been previously reported in the more widely studied alloy, Ti64<sup>[30,51,56]</sup> and was also not seen here in the Ti64 section of the AAC wall made under identical conditions. From the build height-transverse (ND-TD) cross sections, the 3D morphology of these partially refined grains was difficult to interpret. Consequently, a further EBSD map was acquired from the un-peened sample, in the WD-TD plane, which is shown in Figure 14. This reconstructed- $\beta$  phase EBSD map shows that these grains appear nearly equiaxed when sectioned in the WD-TD plane and are thus only elongated in a direction tilted  $\pm 30$  to 50 deg from ND towards TD, as seen in Figure 3(a). By comparison with the etched optical macrographs in Figure 2, it can be seen that near the wall's surfaces this growth direction is near-perpendicular to the convex-curved fusion-boundary bands.<sup>[5,30]</sup> These bands delineate the base of the melt pool surface, which is slightly curved in the core region, where recrystallised grains were observed in the peened samples, but becomes much more highly curved away from ND towards the walls' surfaces. Therefore, since the  $\beta$ -phase  $\langle 001 \rangle_\beta$  dendrites grow fastest parallel to the direction of the maximum thermal gradient<sup>[28,65]</sup> during solidification near the walls' surfaces, some  $\langle 001 \rangle_\beta$  dendrites appear to have become realigned at  $\pm 30$  to 50 deg to ND, to be nearer to normal to the curvature of the solid-liquid melt pool surface, which will have allowed them to develop faster and overgrow the  $\langle 001 \rangle_\beta // \text{ND}$  dendrites. This has led to the establishment of a skin layer of smaller columnar grains with new orientations that have a  $\langle 001 \rangle_\beta$  fibre texture aligned between 30 and 50 deg to ND. This behaviour has also been exemplified in Figure 13, where the  $\beta$  grains have been separated into those represented by the left (b, e) and right (c, f)  $\langle 001 \rangle_\beta // \text{ND}$  texture poles. The more extreme tilt of the  $\beta$  grains in the skin layer near the edge of the wall also confirms that the smaller  $\pm 5$  to 10 deg  $\langle 001 \rangle_\beta // \text{ND}$  split seen consistently in the pole figures taken from the

core of the wall in the peened samples is also due to curvature of the melt pool base. Even though the curvature is less significant in a wall's central region, when finer grains are introduced into each new layer by recrystallisation, it appears growth-selected alignment still occurs to better match the solid-liquid interface profile. In contrast, a split  $\langle 001 \rangle_\beta // \text{ND}$  texture is not normally seen in a normal WAAM Ti64 deposit (e.g., References 23, 56) because, without inducing recrystallisation, after adding multiple layers only a few very large grains survive that have optimised their growth direction to be aligned with their average  $\langle 001 \rangle_\beta$  direction normal to the melt pool solid-liquid surface.

The presence of this refined grain skin layer in all the Ti6242 samples, when it is not seen in Ti64, must also be a consequence of the different alloying elements in this alloy. For example, Mo and Si have partition coefficients of  $k = 2$  and  $k = 0.35$ ,<sup>[26,27,52]</sup> which will create a wider mushy zone, leading to the development of higher-aspect-ratio dendrites, which are more likely to fragment, or reorientate, towards a new crystallographic

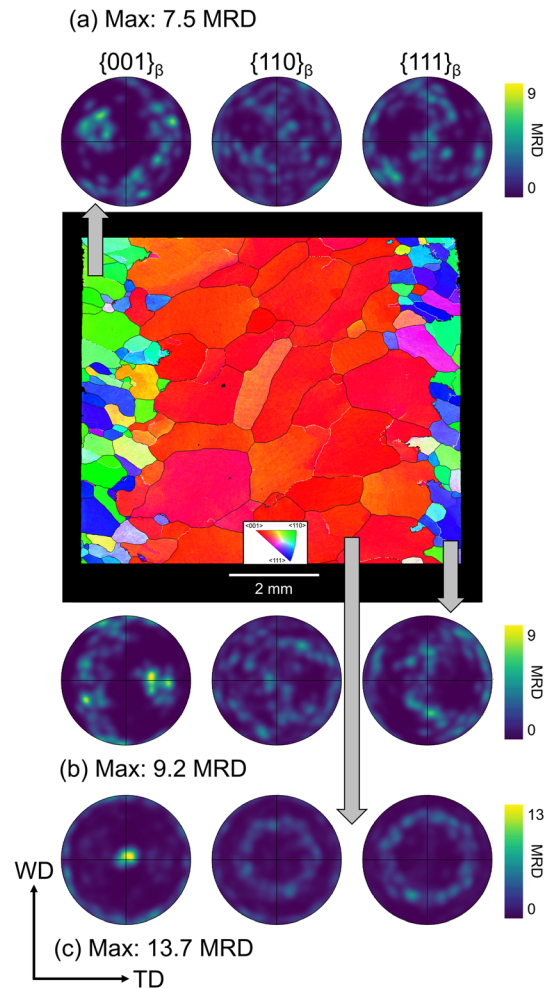


Fig. 14—A top-down EBSD map (WD-TD plane) of the reconstructed  $\beta$ -grain structure of the un-peened Ti6242 sample cross sectioned from the bulk of the WAAM wall. The micro-textures of the (a) left and (b) right-side partially refined grain skin layers, and (c) that of the interior columnar grains are shown in the pole figures.

growth direction, to adjust to the large change in curvature of the melt pool surface near the walls' surfaces.<sup>[28]</sup> A similar behaviour has been reported in Reference 51 where Ti5553 was also added on top of Ti64 by WAAM using the same process parameters, and only the Ti5553 section exhibited a similar skin layer of fine  $\pm 30$  to  $50$  deg tilted  $\langle 001 \rangle_{\beta}$  // ND grains.

## B. Transformation Microstructures

In AM, once a melt tack has solidified, the material subsequently experiences multiple rapid reheating cycles with a diminishing peak temperature. This is an unavoidable consequence of the moving heat source that generates a thermal field containing a steep thermal gradient that is translated across the material in a repeating cycle, which, in a single-track-wide wall is offset by the layer height. For high-deposition-rate processes like WAAM, where the heat source and layer height is significantly larger than in powder-bed processes, this causes the formation of more widely spaced HAZ bands—equivalent to the  $\sim 1$  mm layer height—which are commonly seen in etched optical macrographs.<sup>[5,14–16]</sup> With Ti64 WAAM, the HAZ bands are known to develop by reheating the transformation microstructure that first formed on cooling in the top region of the wall and fully transformed to  $\beta$  in the previous cycle in a thermal gradient through  $T_{\beta}$ . With a moving heat source, the HAZ bands occur where the peak temperatures reached in the thermal gradient below the heat source are in the temperature range of the  $\beta$  approach curve. In this temperature range, the  $\alpha$  phase fraction increasingly reduces with the temperature rise due to regrowth of the residual  $\beta$ . As the peak temperature increases, thinner  $\alpha$  laths in the size distribution thus increasingly disappear, transforming to  $\beta$ , leaving the larger remaining  $\alpha$  lamellae in the  $\beta$  matrix. If the subsequent cooling rate is low enough to suppress  $\alpha$  nucleation, the large surviving  $\alpha$  laths regrow into the  $\beta$  matrix and coarsen, to an extent that increases with rising peak temperature of the thermal cycle. Thus, this will lead to a more rapid coarsening of the  $\alpha$  transformation microstructure in comparison to Ostwald ripening, which is dependent on interfacial energy rather than primarily on the  $\alpha \leftrightarrow \beta$  phase transformation, and is consistent with the observations made by others authors (*e.g.*, References 14–16). In addition, in a thin region where the peak temperature reached is just below  $T_{\beta}$ , only a few  $\alpha$  laths will survive, and due to their wide spacing and the subsequent rapid cooling rate ( $\sim 30$  °C s<sup>-1</sup><sup>[5]</sup>), heterogeneous or autocatalytically biased nucleation of new  $\alpha$  laths will then be favoured in the  $\beta$  matrix over  $\alpha$  regrowth.<sup>[5]</sup> This produces a microstructurally distinct, thin, sublayer at the top of each HAZ band of single-variant  $\alpha$  colonies with a 'packet' type structure.<sup>[5,14–16]</sup> The overall effect on the transformation microstructure is the periodic 'sawtooth' wave pattern variance seen in the  $\alpha$  inter-lamellar spacing in Reference 5 and Figure 9, where in response to each thermal field pass from the heat source (which is offset by the layer height) the inter-lamellar spacing first

increases gradually at lower peak temperatures, and then more rapidly to a maxima, before there is an abrupt change in morphology to the 'packet' colony structure, which exhibits a minima in the lamellar spacing that coincides with the top of each HAZ band.<sup>[5,14–16]</sup>

The as-deposited Ti6242 transformation microstructure followed this same sawtooth wave pattern as Ti64, with respect to its inter-lamellar spacing (Figure 7). In addition, the steady-state part of the wall, which has experienced reheating below  $T_{\beta}$ , also exhibited a similar transformation microstructure morphology to Ti64, with a fine basketweave  $\alpha$  morphology and cyclical coarsening of the  $\alpha$  laths, with a similar 'packet' colony structure seen at the top of each HAZ (Figure 8(d)). This is not surprising given the similarity of the  $\alpha + \beta$  microstructures in the two alloys (*e.g.*, Figures 10(c) and (d)). However, in the Ti64  $\rightarrow$  Ti6242 composite WAAM build (Figure 9), comparable to the behaviour of the  $\beta$ -grain size, the average Ti6242  $\alpha$  inter-lamellar spacing was  $\sim 25$  pct finer than in the Ti64 alloy. This can again be explained by considering the effect of the slowest diffusing species that controls the diffusional transformation rate in each alloy. For Ti64 WAAM, during the initial  $\beta \rightarrow \alpha$  phase transformation, after the cyclic peak temperature first drops below  $T_{\beta}$ , the  $\alpha$  phase nucleates most easily at  $\beta$ -grain boundaries where the energy barrier is lowest, and  $\alpha$  plates form and grow inwards towards the grain centre to produce single variant colonies.<sup>[36,66,67]</sup> However, with the high cooling rate in the WAAM process, a large undercooling rapidly develops and nucleation can then also occur in the grain interiors at dislocations, which leads to the majority of the  $\beta$  grains being transformed to a multi-variant basketweave microstructure.<sup>[28,36]</sup> The growth rate of  $\alpha$  laths at a given undercooling is dependent on partitioning of the slowest diffusing species in each alloy between  $\alpha$  and the  $\beta$  matrix, which will try to maintain equilibrium at the  $\alpha/\beta$  interface.<sup>[60]</sup> The dominant elements that control the  $\alpha$  growth kinetics are thus vanadium for Ti64 and molybdenum for Ti6242.<sup>[26,27,52,53,68]</sup> Given that molybdenum has the slowest diffusivity by far in titanium, the  $\alpha$  plates in Ti6242 will grow more slowly than in Ti64,<sup>[60]</sup> allowing more nucleation and thus an overall finer basketweave microstructure.

It is further worth noting that the whole steady-state region of the Ti6242 wall below the first HAZ band still had, on average, a coarser  $\alpha$  lamellar spacing in Figure 7, compared to the top section that only transformed on cooling from the  $\beta$  phase field and was not reheated. This suggests the temperature fields from each heat source pass overlapped sufficiently in ND to cause significant coarsening of *all* of the  $\alpha$  transformation microstructure, and even that between the HAZ etching lines visible in the optical images, although the extent of coarsening is clearly greater towards the top of each HAZ band, where the etching contrast is visible and the peak temperature was higher. Similar to when the  $\alpha$  initially transformed from  $\beta$ , the coarsening rate on reheating will also be controlled by migration of the  $\alpha/\beta$  interfaces involving diffusion of molybdenum, and this will also be more restricted in Ti6242 than in Ti64, so



that after coarsening the peak inter-lamellar spacing towards the top of the HAZ bands in the Ti6242 are also still reduced in comparison to in Ti64 (Figure 9(c)).

## V. CONCLUSIONS

The  $\beta$ -grain and transformation microstructures produced by the WAAM process in a Ti6242 alloy, with in-process deformation from inter-pass hammer peening, were characterised and directly compared to the ‘workhorse’ titanium alloy, Ti64, produced under identical conditions. The use of inter-pass peening was shown to successfully refine the coarse and columnar  $\beta$ -grain structure in the Ti6242 samples and gave rise to a systematic reduction in the average grain size and texture strength, with decreasing peening pitch and increasing average energy density. A smaller peening pitch also led to an increase in the width of the builds’ core recrystallised regions, seen in transverse cross sections, giving a more homogeneous grain structure.

A Ti64  $\rightarrow$  Ti6242 alloy composite sample was produced to allow direct comparison between the microstructure of Ti6242 and Ti64 under identical process parameters, by switching the feed wire midway through the build height. Analysis of the  $\beta$ -grain size revealed a reduction in average grain diameter across the alloy–alloy transition region and that the recrystallised wall core in Ti6242 was 25 pct more refined than in Ti64. Since the as-solidified  $\beta$  grains in titanium WAAM have the opportunity to substantially coarsen during thermal cycling above the  $\beta$  transus, and grain growth rates depend strongly on solute diffusion, this reduction in grain size between the peened Ti6242 and Ti64 WAAM samples was attributed largely to a difference in grain growth kinetics. In particular, molybdenum, the slowest diffusing solute species in Ti6242, is known to retard  $\beta$ -grain growth and has a significantly lower diffusivity than vanadium, which is the slowest species in Ti64.

With the WAAM process, the  $\alpha$  transformation microstructure in Ti6242 was observed to behave broadly similarly to in Ti64, producing both similar fine lamellar basketweave  $\alpha$  within the  $\beta$  grains, and also a comparable coarsening behaviour on reheating below the  $\beta$  transus, with a similar repeating ‘saw-tooth’ lamellar spacing generated across the HAZ bands by the moving heat source. From analysis of the same Ti64  $\rightarrow$  Ti6242 alloy-alloy composite sample, the  $\alpha$  transformation microstructure was also found to have a 25 pct finer lamellar  $\alpha$  spacing in Ti6242 than in Ti64. This was again attributed to the slower diffusivity of molybdenum solute in Ti6242 that retarded the  $\beta \rightarrow \alpha$  transformation kinetics during cooling and when the material was subsequently thermally cycled by additional melt passes.

Overall, it can be concluded that Ti6242 may be a more suitable alloy for use in high deposition rate wire-AM processes over the ‘workhorse’ alloy Ti64, since it is more resistant to microstructure coarsening during thermal cycling in AM, and it consequently generates a finer as-deposited  $\beta$  and  $\alpha + \beta$

transformation microstructure that can allow a wider range of customisation for mechanical property tailoring through post-build heat treatments.

## ACKNOWLEDGMENTS

The authors are appreciative of the EPSRC programme grants NEWAM (EP/R027218/1) and Light-Form (EP/R001715/1) for supporting aspects of this research. The authors acknowledge the use of equipment associated with the Advanced Metals Processing and Characterisation themes of the Henry Royce Institute for Advanced Materials, funded through EPSRC grants EP/R00661X/1, EP/S019367/1, EP/P025021/1 and EP/P025498/1. P.B. Prangnell is grateful to the Royal Academy of Engineering, UK, and Airbus for supporting his research through the Airbus-University of Manchester Centre for Metallurgical Excellence.

## CONFLICT OF INTEREST

On behalf of all authors, the corresponding author states that there is no conflict of interest.

## OPEN ACCESS

This article is licensed under a Creative Commons Attribution 4.0 International License, which permits use, sharing, adaptation, distribution and reproduction in any medium or format, as long as you give appropriate credit to the original author(s) and the source, provide a link to the Creative Commons licence, and indicate if changes were made. The images or other third party material in this article are included in the article’s Creative Commons licence, unless indicated otherwise in a credit line to the material. If material is not included in the article’s Creative Commons licence and your intended use is not permitted by statutory regulation or exceeds the permitted use, you will need to obtain permission directly from the copyright holder. To view a copy of this licence, visit <http://creativecommons.org/licenses/by/4.0/>.

## REFERENCES

1. S.W. Williams, F. Martina, A.C. Addison, J. Ding, G. Pardal, and P.A. Colegrove: *Mater. Sci. Technol.*, 2016, vol. 32(7), pp. 641–47. <https://doi.org/10.1179/1743284715Y.0000000073>.
2. T. DebRoy, et al.: *Prog. Mater. Sci.*, 2018, vol. 92, pp. 112–224. <https://doi.org/10.1016/j.pmatsci.2017.10.001>.
3. J. Allen: An investigation into the comparative costs of additive manufacture vs. machine from solid for aero engine parts, *Proceedings of the Meeting RTO-MP-AVT-139*, pp. 17-1-17–10, 2006. <https://doi.org/10.14339/RTO-MP-AVT-139-17>.
4. C. Körner: *Int. Mater. Rev.*, 2016, vol. 61(5), pp. 361–77. <https://doi.org/10.1080/09506608.2016.1176289>.
5. A. Ho, H. Zhao, J.W. Fellowes, F. Martina, A.E. Davis, and P.B. Prangnell: *Acta Mater.*, 2019, vol. 166, pp. 306–23. <https://doi.org/10.1016/j.actamat.2018.12.038>.

6. D. Ding, Z. Pan, D. Cuiuri, and H. Li: *Int. J. Adv. Manuf. Technol.*, 2015, vol. 81(1–4), pp. 465–81. <https://doi.org/10.1007/s00170-015-7077-3>.
7. J. Gockel, J. Beuth, and K.M. Taminger: *Addit. Manuf.*, 2014, vol. 1, pp. 119–26. <https://doi.org/10.1016/j.addma.2014.09.004>.
8. K.M. Taminger and R.A. Hafley, Electron beam freeform fabrication for cost effective near-net shape manufacturing, *Specialists' Meeting on Cost Effective Manufacture via Net-Shape Processing (NATO/RTO AVT-139)*, pp. 16:1–10, 2006. <http://ntrs.nasa.gov/search.jsp?R=20060009152%0Ahttps://www.cso.nato.int/pubs/rdp.asp?RDP=RTO-MP-AVT-139>.
9. F. Martina, P.A. Colegrove, S.W. Williams, and J. Meyer: *Metall. Mater. Trans. A Phys. Metall. Mater. Sci.*, 2015, vol. 46(12), pp. 6103–18. <https://doi.org/10.1007/s11661-015-3172-1>.
10. F. Martina, J. Mehnert, S.W. Williams, P.A. Colegrove, and F. Wang: *J. Mater. Process. Technol.*, 2012, vol. 212(6), pp. 1377–86. <https://doi.org/10.1016/j.jmatprotec.2012.02.002>.
11. D. Kovalchuk and O. Ivasishin: *Profile Electron Beam 3D Metal Printing*, Elsevier Inc., Amsterdam, 2019.
12. A.E. Davis, J.R. Kennedy, D. Strong, D. Kovalchuk, S. Porter, and P.B. Prangnell: *Materialia*, 2021, vol. 20(August), p. 101202. <https://doi.org/10.1016/j.mtla.2021.101202>.
13. F. Wang, S.W. Williams, P.A. Colegrove, and A.A. Antonysamy: *Metall. Mater. Trans. A Phys. Metall. Mater. Sci.*, 2013, vol. 44(2), pp. 968–77. <https://doi.org/10.1007/s11661-012-1444-6>.
14. P.A. Kobryn and S.L. Semiatin: *J. Mater. Process. Technol.*, 2003, vol. 135(2–3 SPEC), pp. 330–39. [https://doi.org/10.1016/S0924-0136\(02\)00865-8](https://doi.org/10.1016/S0924-0136(02)00865-8).
15. S.M. Kelly and S.L. Kampe: *Metall. Mater. Trans. A*, 2004, vol. 35A(6), pp. 1861–67. <https://doi.org/10.1007/s11661-004-0095-7>.
16. S.M. Kelly and S.L. Kampe: *Metall. Mater. Trans. A*, 2004, vol. 35A(6), pp. 1869–79. <https://doi.org/10.1007/s11661-004-0095-7>.
17. F. Martina, S.W. Williams, and P.A. Colegrove: *SFF Symp.*, 2013, <https://doi.org/10.1007/s13398-014-0173-7.2>.
18. C.J. Todaro, et al.: *Nat. Commun.*, 2020, vol. 11(1), p. 142. <https://doi.org/10.1038/s41467-019-13874-z>.
19. L. Neto, S.W. Williams, J. Ding, J.R. Hönnige, and F. Martina: *Adv. Surf. Enhanc. 1st Int. Conf. Adv. Surf. Enhanc.*, 2020, vol. 1, pp. 121–32. <https://doi.org/10.1007/978-981-15-0054-1>.
20. K. Zhang, et al.: *Mater. Des.*, 2019, <https://doi.org/10.1016/j.matedes.2019.108191>.
21. M.J. Bermingham, D.H. StJohn, J. Krynen, S. Tedman-Jones, and M.S. Dargusch: *Acta Mater.*, 2019, vol. 168, pp. 261–74. <https://doi.org/10.1016/j.actamat.2019.02.020>.
22. J. Wang, et al.: *J. Alloys Compd.*, 2018, vol. 768, pp. 97–113. <https://doi.org/10.1016/j.jallcom.2018.07.235>.
23. J. Donoghue, A.A. Antonysamy, F. Martina, P.A. Colegrove, S.W. Williams, and P.B. Prangnell: *Mater. Charact.*, 2016, vol. 114, pp. 103–14. <https://doi.org/10.1016/j.matchar.2016.02.001>.
24. X. Zhang, F. Martina, J. Ding, X. Wang, and S.W. Williams: *Fatigue Fract. Eng. Mater. Struct.*, 2017, vol. 40(5), pp. 790–803. <https://doi.org/10.1111/ffe.12547>.
25. A.K. Syed, et al.: *Mater. Sci. Eng. A*, 2021, vol. 814(January), p. 141194. <https://doi.org/10.1016/j.msea.2021.141194>.
26. T. Lyman, *Atlas of Microstructures of Industrial Alloys*. American Society for Metals, 1972.
27. M.J. Bermingham, S.D. McDonald, M.S. Dargusch, and D.H. St. John: *J. Mater. Res.*, 2008, vol. 23(1), pp. 97–104. <https://doi.org/10.1557/jmr.2008.0002>.
28. D.A. Porter and K.E. Easterling, *Phase Transform. Met. Alloys*, vol. 3, 1992.
29. J. Donoghue, et al.: *Acta Mater.*, 2019, vol. 186, pp. 229–41. <https://doi.org/10.1016/j.actamat.2020.01.009>.
30. J.R. Hönnige, et al.: *Metall. Mater. Trans. A*, 2020, vol. 51, pp. 3692–3703.
31. S. Mereddy, M.J. Bermingham, D.H. StJohn, and M.S. Dargusch: *J. Alloys Compd.*, 2017, vol. 695, pp. 2097–2103. <https://doi.org/10.1016/j.jallcom.2016.11.049>.
32. J.R. Kennedy, et al.: *J. Alloys Compd.*, 2022, vol. 895, p. 162735. <https://doi.org/10.1016/j.jallcom.2021.162735>.
33. J.R. Kennedy, A.E. Davis, A.E. Caballero, S.W. Williams, E.J. Pickering, and P.B. Prangnell: *Addit. Manuf.*, 2021, vol. 40(November 2020), p. 101928. <https://doi.org/10.1016/j.addma.2021.101928>.
34. J.R. Kennedy, et al.: *Mater. Lett. X*, 2020, vol. 8, p. 100057. <https://doi.org/10.1016/j.mlblux.2020.100057>.
35. F. Wang, S.W. Williams, and M. Rush: *Int. J. Adv. Manuf. Technol.*, 2011, vol. 57(5–8), pp. 597–603. <https://doi.org/10.1007/s00170-011-3299-1>.
36. G. Lütjering and J.C. Williams: *Titanium*, Springer, Berlin, 2007.
37. D. Lunt, et al.: *Mater. Sci. Eng. A*, 2020, vol. 788, p. 139608. <https://doi.org/10.1016/j.msea.2020.139608>.
38. J. Zhang, X. Wang, S. Paddea, and X. Zhang: *Mater. Des.*, 2016, vol. 90, pp. 551–61. <https://doi.org/10.1016/j.matdes.2015.10.141>.
39. C. Hicks, T. Konkova, and P. Blackwell: *Mater. Charact.*, 2020, vol. 170(February), p. 110675. <https://doi.org/10.1016/j.matchar.2020.110675>.
40. I. Burkhardt, R. Visone, S. Riekehr, M.W. Rackel, N. Kashaev, and J. Enz: *Procedia CIRP*, 2018, vol. 74, pp. 176–79. <https://doi.org/10.1016/j.procir.2018.08.088>.
41. P. Harish, Understanding the Effect of Isothermal Heat Treatments on Microstructure of LMD-w Titanium Alloy (Ti-6242), University West, 2020.
42. ASM International, *Materials Properties Handbook: Titanium Alloys*. Materials Park, OH, 1994.
43. TIMET, “TIMETAL 6-2-4-2 (datasheet),” 2000. <https://www.timet.com/assets/local/documents/datasheets/alphaalloys/6242.pdf>. Accessed 09 Oct 2021.
44. M.-L. Antti, V.C. Ciprés, J. Mouzon, P. Åkerfeldt, and R. Pederson, Effect of silicon on creep proper es of titanium 6Al-2Sn-4Zr-2Mo alloy, *14th World Conference on Titanium*, 2020. <https://doi.org/10.1051/mateconf/202032104021>.
45. J.D. Cotton, et al.: *JOM*, 2015, vol. 67(6), pp. 1281–1303. <https://doi.org/10.1007/s11837-015-1442-4>.
46. G. Lütjering: *Mater. Sci. Eng. A*, 1998, vol. 243(1–2), pp. 32–45. [https://doi.org/10.1016/s0921-5093\(97\)00778-8](https://doi.org/10.1016/s0921-5093(97)00778-8).
47. A.K. Singh and C. Ramachandra: *J. Mater. Sci.*, 1997, vol. 32(1), pp. 229–34. <https://doi.org/10.1023/A:1018516324856>.
48. H. Zhao, A. Ho, A.E. Davis, A.A. Antonysamy, and P.B. Prangnell: *Mater. Charact.*, 2019, vol. 147(July), pp. 131–45. <https://doi.org/10.1016/j.matchar.2018.10.027>.
49. P.S. Davies, An investigation of microstructure and texture evolution in the Near- $\alpha$  titanium alloy Timetal 834, University of Sheffield, 2009.
50. P.S. Davies, B.P. Wynne, W.M. Rainforth, M.J. Thomas, and P.L. Threadgill: *Metall. Mater. Trans. A Phys. Metall. Mater. Sci.*, 2011, vol. 42(8), pp. 2278–89. <https://doi.org/10.1007/s11661-011-0606-2>.
51. J.R. Kennedy, et al.: *Mater. Charact.*, 2021, vol. 182(October), p. 111577. <https://doi.org/10.1016/j.matchar.2021.111577>.
52. H. Okamoto and H. Okamoto: *Phase Diagrams for Binary Alloys*, ASM international, Materials Park, 2000.
53. M.J. Bermingham, S.D. McDonald, D.H. StJohn, and M.S. Dargusch: *J. Alloys Compd.*, 2009, vol. 481(1–2), pp. 20–23. <https://doi.org/10.1016/j.jallcom.2009.03.016>.
54. A.E. Davis, et al.: *Mater. Sci. Eng. A*, 2019, <https://doi.org/10.1016/j.msea.2019.138289>.
55. T. Ahmed and H.J. Rack: *Mater. Sci. Eng. A*, 1998, vol. 243, pp. 206–11. [https://doi.org/10.1016/S0921-5093\(97\)00802-2](https://doi.org/10.1016/S0921-5093(97)00802-2).
56. A.E. Davis, J.R. Kennedy, J. Ding, and P.B. Prangnell: *Mater. Charact.*, 2020, vol. 163(February), p. 110298. <https://doi.org/10.1016/j.matchar.2020.110298>.
57. A. Kumar, T. Jayakumar, B. Raj, and D. Banerjee: *Philos. Mag.*, 2008, vol. 88(3), pp. 327–38. <https://doi.org/10.1080/14786430701837015>.
58. J.W. Lu, Y.Q. Zhao, P. Ge, and H.Z. Niu: *Mater. Charact.*, 2013, vol. 84(96), pp. 105–11. <https://doi.org/10.1016/j.matchar.2013.07.014>.
59. S.L. Semiatin, J.C. Soper, and I.M. Sukonnik: *Acta Metall.*, 1996, vol. 44(5), pp. 1979–1986. [https://doi.org/10.1016/1359-6454\(95\)03111-8](https://doi.org/10.1016/1359-6454(95)03111-8).
60. A.K. Ackerman, et al.: *Metall. Mater. Trans. A Phys. Metall. Mater. Sci.*, 2020, vol. 51(1), pp. 131–41. <https://doi.org/10.1007/s11661-019-05472-x>.
61. A.E. Davis, A.E. Caballero, and P.B. Prangnell: *Materialia*, 2020, <https://doi.org/10.1016/j.mtla.2020.100857>.
62. J.W. Cahn: *Acta Metall.*, 1962, vol. 10(9), pp. 789–98. [https://doi.org/10.1016/0001-6160\(62\)90092-5](https://doi.org/10.1016/0001-6160(62)90092-5).



63. F.J. Humphreys and M. Hatherly: *Recrystallization and Related Annealing Phenomena*, Elsevier, Oxford, 1996.
64. W.F. Gale and T.C. Totemeier, eds.: *Smithells Metals Reference Book*, 8th ed. Elsevier & ASM International, Oxford, 2004.
65. S.A. David and J.M. Vitek: *Int. Mater. Rev.*, 1989, vol. 34(1), pp. 213–45. <https://doi.org/10.1179/imr.1989.34.1.213>.
66. Y. Ohmori, K. Nakai, H. Ohtsubo, and M. Tsunofuri: *Mater. Trans. JIM*, 1994, vol. 35(4), pp. 238–46. <https://doi.org/10.2320/matertrans1989.35.238>.
67. A.E. Davis, J. Donoghue, J.R. Kennedy, N. Byres, and P.B. Prangnell: *Acta Mater.*, 2021, vol. 220, p. 117315. <https://doi.org/10.1016/j.actamat.2021.117315>.
68. H. Okamoto: *J. Phase Equilib. Diffus.*, 2000, vol. 21(3), p. 311.

**Publisher's Note** Springer Nature remains neutral with regard to jurisdictional claims in published maps and institutional affiliations.